



저작자표시-비영리-변경금지 2.0 대한민국

이용자는 아래의 조건을 따르는 경우에 한하여 자유롭게

- 이 저작물을 복제, 배포, 전송, 전시, 공연 및 방송할 수 있습니다.

다음과 같은 조건을 따라야 합니다:



저작자표시. 귀하는 원저작자를 표시하여야 합니다.



비영리. 귀하는 이 저작물을 영리 목적으로 이용할 수 없습니다.



변경금지. 귀하는 이 저작물을 개작, 변형 또는 가공할 수 없습니다.

- 귀하는, 이 저작물의 재이용이나 배포의 경우, 이 저작물에 적용된 이용허락조건을 명확하게 나타내어야 합니다.
- 저작권자로부터 별도의 허가를 받으면 이러한 조건들은 적용되지 않습니다.

저작권법에 따른 이용자의 권리는 위의 내용에 의하여 영향을 받지 않습니다.

이것은 [이용허락규약\(Legal Code\)](#)을 이해하기 쉽게 요약한 것입니다.

[Disclaimer](#)

공학석사 학위논문

Effects of Flow Coefficient on Unsteady Impeller Loading

유량 계수가 임펠러 비정상 하중에 미치는 영향

2018년 2월

서울대학교 대학원

기계항공공학부

공 동 재

Effects of Flow Coefficient on Unsteady Impeller Loading

지도 교수 송 성 진

이 논문을 공학석사 학위논문으로 제출함
2018년 2월

서울대학교 대학원
기계항공공학부
공 동 재

공동재의 공학석사 학위논문을 인준함
2018년 2월

위 원 장 _____ 박 형 민 _____ (인)

부위원장 _____ 송 성 진 _____ (인)

위 원 _____ 황 원 태 _____ (인)

Abstract

Effects of Flow Coefficient on Unsteady Impeller Loading

Dongjae Kong

School of Mechanical and Aerospace Engineering

The Graduate School

Seoul National University

Unsteady Reynolds-Averaged Navier-Stokes (URANS) simulation has been conducted to investigate how flow coefficient affects unsteady impeller loading. Simulations have been carried out at three flow coefficients - near stall, design, and near choke conditions - for two radial gaps (1.04 and 1.10). For computational efficiency, the unsteady simulation has been conducted for two impeller and diffuser passages via Fourier Transformation method. Both steady and unsteady simulations have been validated against experimental data. For the radial gap of 1.04, the unsteady loading (the difference between the maximum and minimum loadings) is the largest at the near stall condition; second largest at the near choke condition; and smallest at the design condition. Flow coefficient effects on the unsteady impeller loading are mostly due to the variations in pressure fluctuations on the pressure side of the impeller blade. Relative to the design condition, the near stall condition shows lower minimum loading and the near choke condition shows higher

maximum loading. Therefore, both off design conditions result in higher unsteady loading than the design condition. Such differences stem from the variations in the pitch-wise static pressure at the diffuser vane inlet caused by the flow incidence onto the diffuser vanes. For the radial gap of 1.10, unsteady impeller loading decreases at three flow coefficients compared to that of the radial gap of 1.04. In addition, flow coefficient has a negligible effect on the unsteady impeller loading. Such independence stems from the attenuated potential effect of the diffuser vane with the radial gap increase.

Keywords : Centrifugal compressor, Flow coefficient, Unsteady CFD, Unsteady loading

Student Number : 2016-20668

Table of Contents

Abstract	i
Table of Contents	iii
List of Figures	v
List of Tables	vii
Nomenclature	viii
Chapter 1. Introduction	1
1.1. Research Background	1
1.2. Previous Research.....	3
1.3. Research Motivation and Objectives	6
Chapter 2. Test Compressor	8
2.1. Geometry	8
2.2. Measurements	10
Chapter 3. Numerical Simulation	12
3.1. Grid.....	12
3.2. Numerical Methods	15
3.2.1. Steady Simulation	15
3.2.2. Unsteady Simulation	17
3.3. Numerical Method Validation.....	20
3.3.1. Grid Dependence Test	20
3.3.2. Compressor Map	21
3.3.3. Periodicity of Unsteady Simulation	23

3.3.4. Diffuser Vane Inlet Time Averaged Velocity Contour	25
3.3.5. Diffuser Vane Inlet Temporal Velocity Variation	27
Chapter 4. Results and Discussions.....	29
4.1. Radial gap of 1.04.....	29
4.1.1. Chord-wise Unsteady Loading Distribution.....	29
4.1.2. Origin of Unsteady Loading.....	32
4.1.3. Fast Fourier Transformation Analysis	38
4.1.4. Loading and Pressure Fluctuations.....	39
4.1.5. Diffuser Vane Inlet Pressure Distribution.....	44
4.2. Radial gap of 1.10.....	49
4.2.1. Chord-wise Unsteady Loading Distribution.....	49
4.2.2. Fast Fourier Transformation Analysis	52
4.2.3. Loading and Pressure Fluctuations.....	53
4.2.4. Diffuser Vane Inlet Pressure Distribution.....	57
Chapter 5. Conclusions	59
Bibliography.....	61
Abstract in Korean	64

List of Figures

Figure 1.1 Vaneless diffuser	2
Figure 1.2 Vaned diffuser	2
Figure 1.3 Schematic of impeller-diffuser interaction.....	3
Figure 2.1 Frontal view of the centrifugal compressor stage.....	9
Figure 2.2 Measurement planes.....	11
Figure 3.1 Impeller passage grid	13
Figure 3.2 Diffuser passage grid.....	14
Figure 3.3 Computational domain of the steady simulation.....	16
Figure 3.4 Computational domain of the unsteady simulation	18
Figure 3.5 Grid dependence results	20
Figure 3.6 Comparison of compressor map	22
Figure 3.7 Pressure periodicities at six monitoring points.....	24
Figure 3.8 Diffuser vane inlet time averaged velocity contours	26
Figure 3.9 Diffuser vane inlet velocity variations with respect to time at four measurement points	28
Figure 4.1 Chord-wise distributions of unsteady loading per unit span.....	31
Figure 4.2 Normalized static pressure contours and loading fluctuations at the design condition and 10% span-wise location	37
Figure 4.3 Frequency contents of the unsteady loading at 0.98 chord-wise	

coordinate location	38
Figure 4.4 Chord-wise distributions of pressure side pressure fluctuations, suction side pressure fluctuations, and loading fluctuations at near stall, design, and near choke conditions	42
Figure 4.5 Pitch-wise time averaged static pressure distributions at $r/r_2 = 1.039$.....	45
Figure 4.6 Time averaged diffuser vane inlet pressure fields	48
Figure 4.7 Velocity triangles of impeller exit flow at three flow coefficients	48
Figure 4.8 Chord-wise distributions of unsteady loading per unit span.....	51
Figure 4.9 Frequency contents of the unsteady loading at 0.98 chord-wise coordinate location	52
Figure 4.10 Chord-wise distributions of pressure side pressure fluctuations, suction side pressure fluctuations, and loading fluctuations at near stall, design, and near choke conditions	56
Figure 4.11 Pitch-wise time averaged static pressure distributions at $r/r_2 = 1.099$.....	58
Figure 4.12 Schematic of the influence of flow coefficient on the unsteady impeller loading	58

List of Tables

Table 2.1 Geometrical Specifications	9
Table 2.2 Test conditions	10
Table 3.1 Locations of monitoring points for periodicity.....	19
Table 4.1 Maximum unsteady loading at three flow coefficients and three span-wise locations	30
Table 4.2 Maximum unsteady loading at three flow coefficients and three span-wise locations	51

Nomenclature

b	Diffuser vane height
C	Absolute velocity
C_P	Static pressure coefficient
DV	Diffuser vane
L_{DVPS}	Length of vane pressure side
L_{DVSS}	Length of vane suction side
N	Shaft speed
N_D	Diffuser vane number
N_I	Impeller blade number
P	Pressure
PS	Pressure side
P_T	Total pressure
Q	Volume flow rate
r	Radial coordinate (= radius)
s	Stream-wise coordinate (= chord-wise coordinate)
SS	Suction side
T	Diffuser vane passing period
t	Time
T_t	Total temperature
U_{tip}	Impeller tip speed
W	Relative velocity
z	Axial coordinate
α_{4SS}	Diffuser vane angle
α_{DV}	Diffuser vane wedge angle
β_b	Impeller back-sweep angle at the exit
γ	Specific heat ratio
ΔP	Loading (= $P_{PS} - P_{SS}$)
η_c	Isentropic efficiency

θ	Circumferential coordinate
θ_D	Diffuser vane pitch
π_{tc}	Total pressure ratio
ρ	Density
τ_{tc}	Total temperature ratio
ϕ	Flow coefficient ($= Q/(\Omega r_2^3)$)
Ω	Angular speed

Subscripts

2	Impeller exit
4	Diffuser vane inlet
4M	4M Measurement location
8M	8M Measurement location
max	Maximum
min	Minimum

Superscripts

-	Time average
'	Fluctuation

Chapter 1. Introduction

1.1. Research Background

Centrifugal compressors have wide applications like aircraft propulsion, automotive transportation, and process applications. Compared to axial machines, centrifugal compressors are more compact and achieve higher pressure rise per stage. A centrifugal compressor stage consists of an impeller and a diffuser. Impeller rotates and pressure rise inside the impeller comes from the centrifugal force. Diffuser is a stationary part which is located next to the impeller and pressure rise inside the diffuser comes from the diffusion mechanism. Area in the diffuser increases in radial direction, and, thus, diffusion occurs in radial direction. Diffuser may be vaneless (Fig. 1.1) or vaned (Fig. 1.2), and diffuser vanes are installed to enhance pressure rise and efficiency removing swirl component of the velocity more rapidly. While diffuser vanes offer aerodynamic benefits, the relative motion between the rotating impeller and the stationary diffuser vanes leads to impeller-diffuser interaction. In axial machines, it is also known as rotor-stator interaction. Upstream component is affected by the potential effect of the downstream component and the downstream component is affected by the upstream wake.

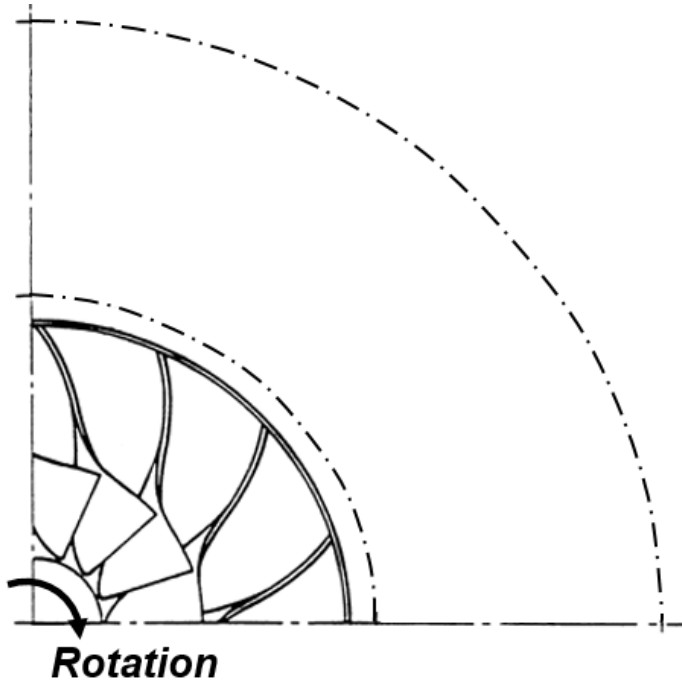


Figure 1.1. Vaneless diffuser.

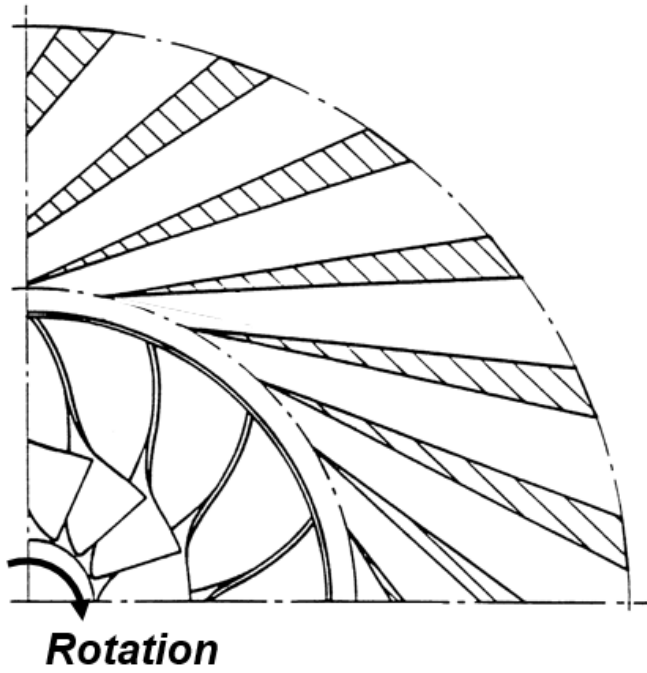
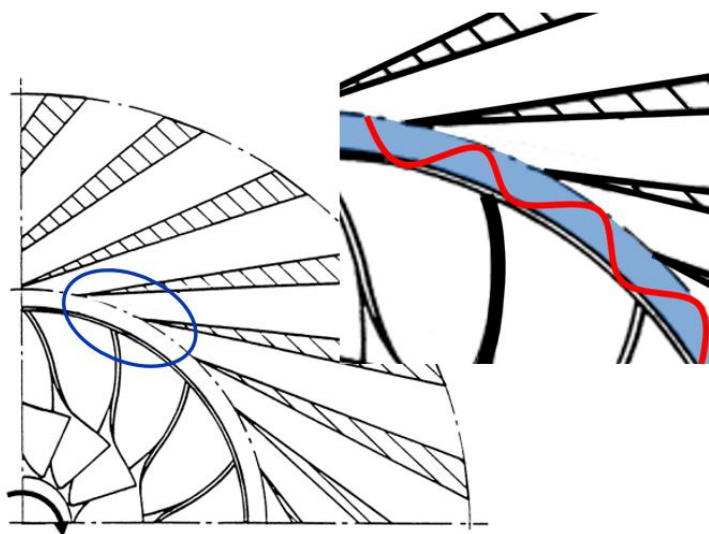


Figure 1.2. Vaned diffuser.

1.2. Previous Research

Impeller-diffuser interaction has been mainly studied from the aerodynamic performance perspective. Ziegler et al. [1, 2] conducted an experimental investigation of the effects of impeller-diffuser interaction on the aerodynamic performance using both steady and unsteady measurements. Shum et al. [3] reported effects of radial gap on the impeller performance with numerical simulation and suggested a radial gap which optimizes the impeller performance.

However, the impeller-diffuser interaction can also cause vibration of compressor components. The potential effect of the diffuser vane imposes a non-uniform pressure field in the vaneless space, resulting in unsteady loading for the rotating impeller blades (Fig. 1.3). Thus, impeller is subject to the unsteady as well as the static loading and can be vulnerable to vibration.



Rotation

Figure 1.3. Schematic of impeller-diffuser interaction.

Several studies have been conducted to understand and predict unsteady impeller loading induced by impeller-diffuser interaction. In a low-speed centrifugal compressor, Sanders and Fleeter [4] measured unsteady impeller loadings at three flow coefficients and reported that the unsteady impeller loading decreased with increasing flow coefficient. Studies have also been conducted in high-speed centrifugal compressors. Gaetani et al. [5, 6] measured unsteady static pressure, Mach number, and flow angle in the vaneless space using Fast Response Aerodynamic Pressure Probes. Smythe [7] numerically investigated unsteady impeller loading in two different compressors at two flow coefficients (near design and lower than the design flow coefficients). One had a larger impeller tip radius and a smaller radial gap than the other. The impeller with a larger tip radius (thus, smaller radial gap between the impeller and the diffuser) showed increased unsteady loading on the impeller and such unsteady loading was concentrated at the trailing edge of the blade. Smythe also reported that the unsteady impeller loading decreased at the higher flow coefficient. For the same geometries and operating conditions, Villanueva [8] reported that the unsteady impeller loading is set by the “difference in static pressure from the pressure surface to the suction surface at the leading edge of the diffuser vane”, and such difference increases as the diffuser vane incidence decreases or flow coefficient increases. Gould et al. [9] conducted a quasi-two-dimensional numerical simulation and reported that the downstream disturbance induced by the diffuser vane was attenuated more rapidly when the relative Mach

number inside the impeller passage increased.

Srivastava et al. [10] numerically calculated the impeller strains, and the analysis showed a periodic shock impingement on the impeller blade pressure side due to the impeller-diffuser interaction. The first harmonic of the diffuser vane passing period in the unsteady pressure was used to calculate the structural stability of the impeller. Zemp and Abhari [11] measured impeller blade stress levels induced by the impeller-diffuser interaction using dynamic strain gauges. The stress measurements were conducted at the design and off-design (near stall and near choke) conditions for two radial gaps of 1.08 and 1.13. The maximum stress level decreased with increasing flow coefficient for the large radial gap (1.13). However, for the smaller radial gap (1.08), the maximum stress levels were larger at both off-design conditions relative to the design condition.

1.3. Research Motivation and Objectives

As centrifugal compressor operates at various operating conditions, unsteady impeller loading and its effects on the structure at various operating conditions need to be understood. Measurements of Sanders and Fleeter [4] were conducted in a low-speed compressor and did not cover a wide range of operating conditions. In addition, results from previous studies in high-speed compressors ([7, 8] and [11]) are inconsistent. Based on investigation at two flow coefficients (near design and lower than the design flow coefficients), Smythe [7] found that the unsteady impeller loading decreases with increasing flow coefficient. According to Villanueva [8]'s argument, unsteady impeller loading can be expected to continuously decrease as the flow coefficient increases to near choke condition. However, Zemp and Abhari [11] found that the maximum impeller stress has a local minimum at the design condition and be relatively higher at the off-design (near stall and near choke) conditions. Therefore, there is a still a need for a systematic investigation of the effects of flow coefficient on the unsteady impeller loading induced by the impeller-diffuser interaction in a high-speed compressor. In addition, as the radial gap is a key design parameter, such investigation should be conducted at various radial gaps. To address this need, this paper presents results from a numerical investigation. Specific research questions to be answered can be summarized as:

1. How does the flow coefficient affect unsteady impeller loading?
2. Why does the flow coefficient affect unsteady impeller loading?
3. How does the radial gap influence on the effects of flow coefficient on the unsteady impeller loading?

Chapter 2. Test Compressor

2.1. Geometry

The current study has been conducted on the open test case “Radiver”. The measurement on the test case were carried out at the Institute of Jet Propulsion and Turbomachinery at RWTH Aachen, Germany. Part of the investigations was funded by the Deutsche Forschungsgemeinschaft (DFG). Figure 2.1 is the frontal view of the centrifugal compressor stage. It is composed of an unshrouded impeller with 15 backswept main blades and 23 wedged-type diffuser vanes. Diffuser vane allows an adjustment of diffuser vane angle, α_{4SS} , and radial gap, r_4/r_2 . For the current study, diffuser vane angle has been set as 16.5° and two radial gaps, 1.04 and 1.10, have been investigated. Geometrical specifications are summarized in Table 2.1. The design point and other test conditions are listed in Table 2.2 for each radial gap. For the radial gap of 1.04, flow coefficients of 0.2073, 0.2232, and 0.2362 corresponding to near stall, design, and near choke conditions, respectively, have been analyzed. For the radial gap of 1.10, flow coefficients of 0.2077, 0.2236, and 0.2429 corresponding to near stall, design, and near choke conditions, respectively, have been analyzed. Flow coefficients near stall and design are similar between two radial gaps. However, radial gap of 1.10 has a larger near choke flow coefficient than radial gap of 1.04. As radial gap increases, throat area in the diffuser vane passage increases due to

kinematics. Thus, radial gap of 1.10 has a larger near choke flow coefficient than radial gap of 1.04.

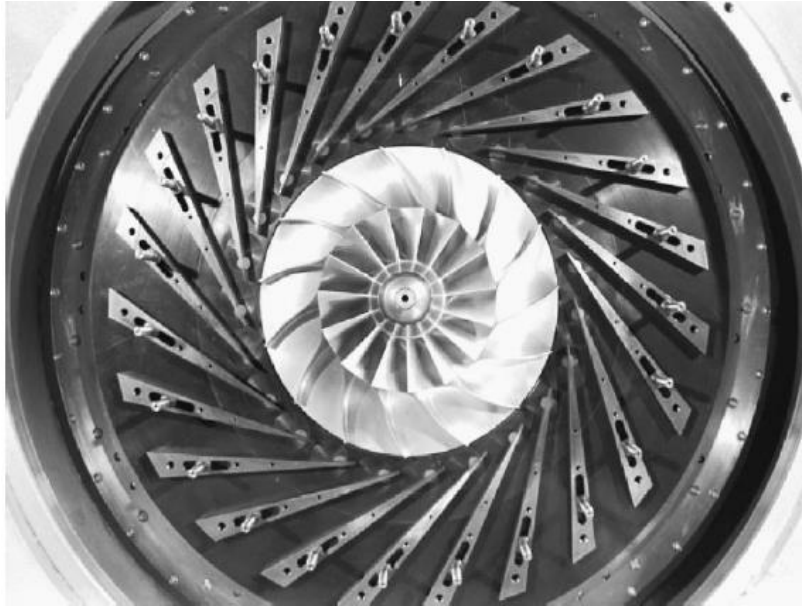


Figure 2.1. Frontal view of the centrifugal compressor stage [1].

Table 2.1. Geometrical specifications [1].

Impeller	
Tip radius, r_2	135 mm
Number of blades, N_I	15
Blade back-sweep angle at the exit, β_b	38°
Diffuser	
Height, b	11.1 mm
Number of vanes, N_D	23
Diffuser vane angle, α_{4SS}	16.5°
Radial gap, r_4/r_2	1.04
	1.10
Diffuser vane wedge angle, α_{DV}	6.615°
Length of vane pressure side, L_{DVPS}	178 mm
Length of vane suction side, L_{DVSS}	190 mm

Table 2.2. Test conditions.

Shaft speed, N	28160 RPM
Impeller tip speed, U_{tip}	398.4 m/s
Radial gap	1.04
Near stall flow coefficient	0.2073
Design flow coefficient	0.2232
Near choke flow coefficient	0.2362
Radial gap	1.10
Near stall flow coefficient	0.2077
Design flow coefficient	0.2236
Near choke flow coefficient	0.2429

2.2. Measurements

Measurement methods from “Radiver” are briefly cited here. Although steady and unsteady measurements were conducted extensively at various locations, only the measurement locations relevant to the current study are described. Figures 2.2 (a) and (b) represent the frontal and the meridional views of measurement planes, respectively. Steady measurements at the 8M location were conducted with a 3-hole cylinder probe, temperature probe, and pressure taps. Unsteady measurements at the 4M location were conducted using time-resolved Laser-2-Focus technique. Aforementioned measurements were conducted at the 80% of the shaft speed, and, thus, numerical simulation of the current study has been conducted at the same shaft speed. More details of the test rig and measurement techniques can be found in [1, 2].

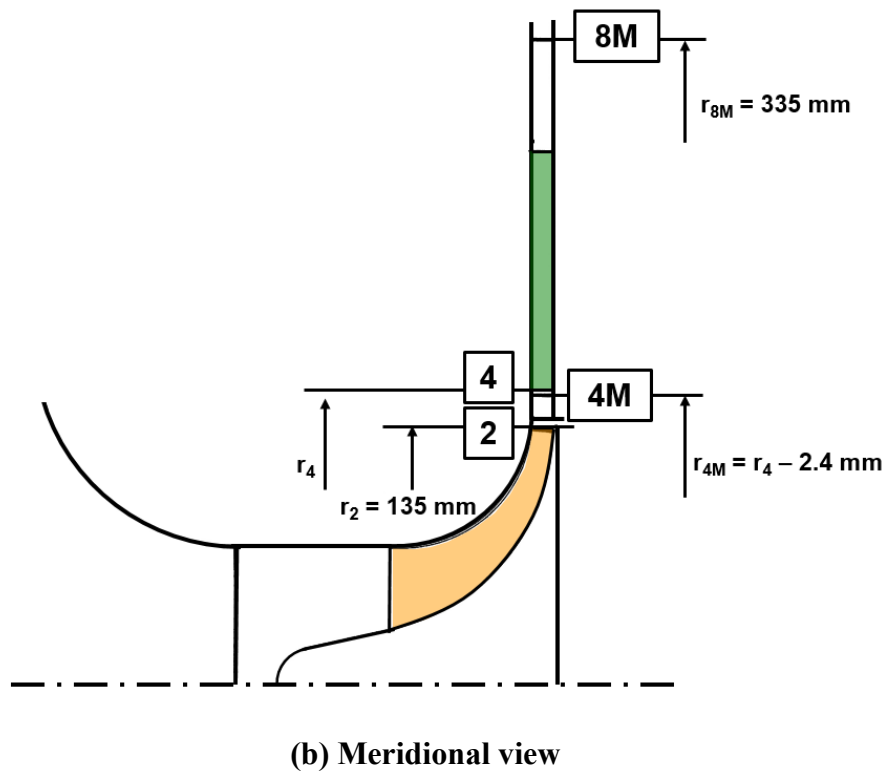
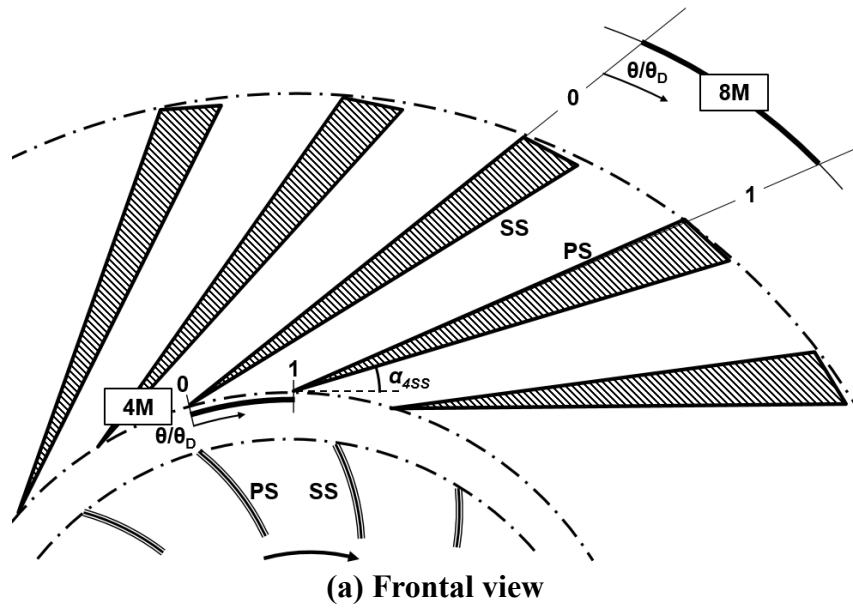


Figure 2.2. Measurement planes [1, 2].

Chapter 3. Numerical Simulation

3.1. Grid

Computational domain and grid have been generated using ANSYS Turbogrid 17.0. Inlet of the computational domain is located twice the impeller leading edge tip radius upstream from the impeller leading edge. Diffuser vane exit and outlet radii are located at 1.97 and 2.67 times the impeller trailing edge tip radius, respectively. The collector has not been modeled since it has a spiral shape, and, thus, no rotational periodicity can be applied. Locations of the inlet and the outlet have been selected to minimize the effects of boundaries on the computation. Structured and hexahedral grid has been adopted.

Figure 3.1 shows a grid for a single impeller passage. Overall grid distribution and grid distributions at specific regions are presented. Specific regions are: (1) near the leading edge; (2) tip clearance; and (3) near the trailing edge. Tip clearance of the unshrouded impeller is a crucial parameter which determines internal flow characteristics of the impeller passage, and, thus, affects flow characteristics in the following diffuser passage. The tip clearance of the current impeller is uniformly 0.7 mm when cold. However, as the compressor accelerates, centrifugal force and hot air affect tip clearance distribution, and Ziegler [12] predicted the hot condition tip clearance distribution via FEM analysis. Both polynomial and linear tip clearance

distributions were suggested and the maximum difference of the tip clearance between the linear distribution and the polynomial distribution was 0.025 mm. Thus, for the simplicity, the current study has adopted the linear tip clearance distribution suggested in [12], and, thus, tip clearances at the leading and the trailing edges have been set at 0.69 mm and 0.48 mm, respectively. Grid number in span-wise direction has been set as 10 for the tip clearance region.

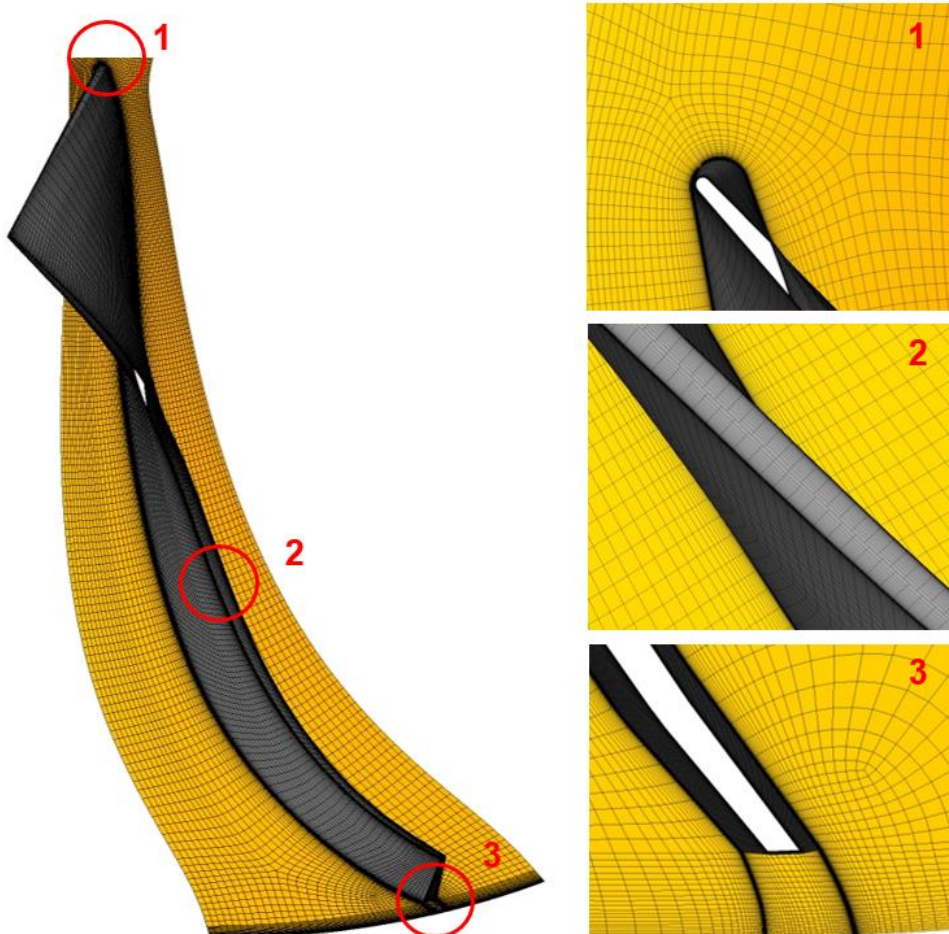


Figure 3.1. Impeller passage grid.

Figure 3.2 shows a grid distribution of a single diffuser passage. Overall grid distribution and grid distributions at specific regions are presented. Specific regions are: (1) near the leading edge and (2) near the trailing edge. Leading edge of the diffuser vane has wedge thickness of 0.45 mm and it has been generated in the numerical simulation.

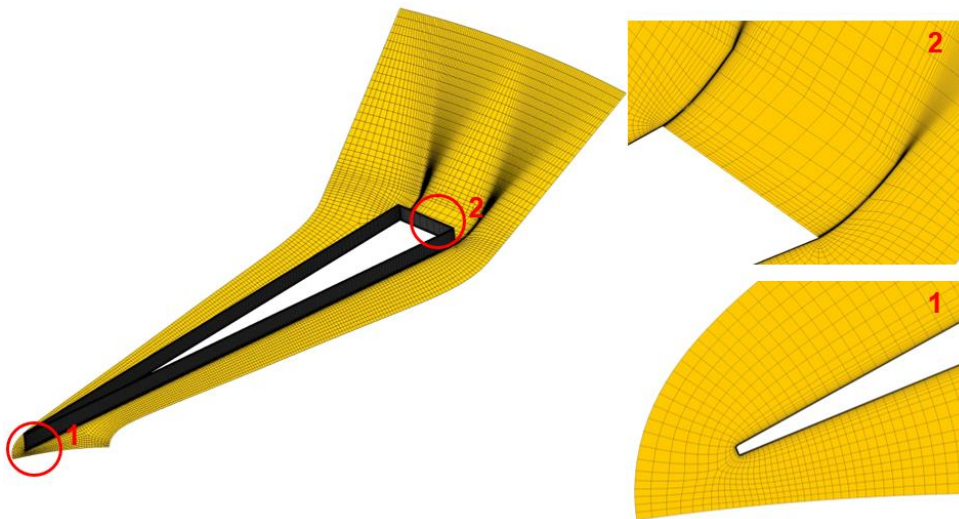


Figure 3.2. Diffuser passage grid.

3.2. Numerical Methods

3.2.1. Steady Simulation

Both steady and unsteady three-dimensional Reynolds-Averaged Navier-Stokes (RANS) simulations have been carried out using ANSYS CFX 17.0. Steady simulations have been conducted to obtain the initial condition for the unsteady simulation. Uniform total pressure and total temperature have been imposed at the inlet boundary. In addition, inlet flow direction and turbulence intensity of 5% have been imposed. The mass flow rate has been set at the outlet boundary, and air as ideal gas has been used as the working fluid. Total energy modeling has been adopted for the heat transfer calculation, and viscous work has been included. Wall has been modeled as an adiabatic smooth surface with no slip. Shear Stress Transport (SST) model has been utilized and y^+ the near wall grid has been maintained around unity. Additional options for the SST model have also been activated. Reattachment Modification (RM) has been used to enhance the turbulence levels in the separating shear layers emanating from walls. In addition, curvature correction has been implemented to modify turbulence production under the streamline curvature and system rotation conditions. Flow has been assumed to be fully turbulent and transition from the laminar flow to the turbulent flow has not been considered.

Steady simulation has been conducted for a single passage of the impeller and the diffuser. Rotationally periodic boundary conditions have been

imposed on the pitch-wise periodic interfaces for the impeller and the diffuser. The impeller-diffuser interface has been modeled via the mixing plane method. Mixing plane method transports circumferentially averaged physical quantities to the following domain. Therefore, it loses circumferential non-uniformity while maintains axial non-uniformity. The interface is equidistant from the impeller trailing edge and the diffuser vane leading edge regardless of the radial gap. Root mean square (RMS) of the residuals below 10^{-4} has been selected as a converged solution. Figure 3.3 shows computational domain of the steady simulation. Inlet, outlet boundaries and interface between the impeller domain and the diffuser domain are marked.

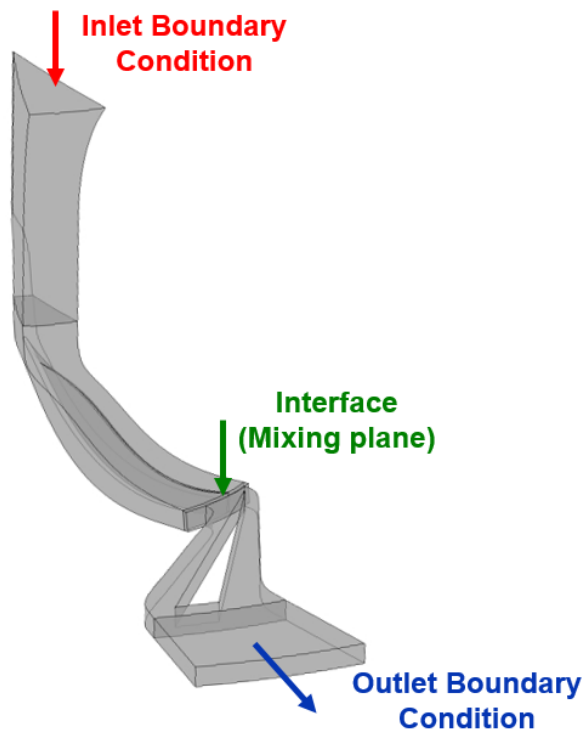


Figure 3.3. Computational domain of the steady simulation.

3.2.2. Unsteady Simulation

Using the steady simulation results as the initial condition, unsteady simulations have been conducted. For structural reasons, the pitch ratio between the impeller and the diffuser is not unity (15/23). Such unequal pitch ratio problem can be solved with full annulus simulation. However, it requires large amount of computational resources. Therefore, the current study adopted Transient Blade Row model to enhance computational efficiency. Transient Blade Row model in ANSYS CFX 17.0 has three sub-models which are Profile Transformation, Time Transformation, and Fourier Transformation. Among them, Fourier Transformation method has been utilized for the current study, and, thus, two passages of the impeller and the diffuser have been modeled. Figure 3.4 shows a computational domain for the unsteady simulation. Inlet, outlet boundaries and interface between the impeller domain and the diffuser domain are marked.

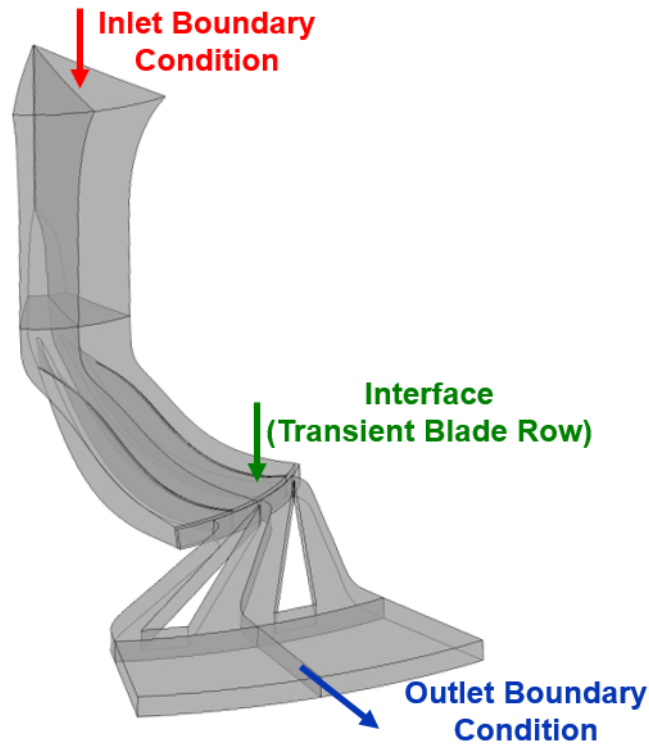


Figure 3.4. Computational domain of the unsteady simulation.

The basic principle of the Fourier transformation is to extend rotational periodicity (as in steady simulation) to account for the phase shifted physical quantities. The Fourier Transformation utilizes temporal Fourier decomposition on the pitch-wise periodic interfaces and temporal-circumferential Fourier decomposition at the rotating-stationary domains interface. The key benefits from the Fourier Transformation method are its applicability to turbomachinery regardless of the pitch ratio and applicability for multi-stage modeling. More detailed technical discussions on the Transient Blow Row model and Fourier Transformation method can be found in [13, 14]. Time step for the unsteady simulation has been set to be 1/30 of the diffuser vane pitch which corresponds to 0.52 degree rotation for each

time step. In the unsteady simulations, in addition to the residuals' RMS, periodicity coefficients (Eq. (3.1)) under 0.5% have also been used as convergence criteria. Periodicity coefficients have been evaluated at six points near the impeller trailing edge and specific locations are tabulated in Table 3.1.

$$\begin{aligned} \text{Periodicity coefficient [\%]} \\ = \frac{P(r, \theta, z, t + T) - P(r, \theta, z, t)}{P(r, \theta, z, t)} \times 100 \quad (3.1) \end{aligned}$$

Table 3.1 Locations of monitoring points for periodicity.

Monitoring point	Location
Point 1	Pressure side & 10% Span (near hub)
Point 2	Suction side & 10% Span (near hub)
Point 3	Pressure side & 50% Span (mid span)
Point 4	Suction side & 50% Span (mid span)
Point 5	Pressure side & 90% Span (near shroud)
Point 6	Suction side & 90% Span (near shroud)

3.3. Numerical Method Validation

3.3.1. Grid Dependence Test

Figure 3.5 shows plots of the total pressure ratio versus grid number for the radial gap of 1.04. For three flow coefficients, total pressure ratio from the inlet to the 8M location (Fig. 2.2) has been investigated for various grid numbers. Grid number is the sum of the grids in the single passage of the impeller and the diffuser. At all flow coefficients, total pressure ratio change is negligible between grid number of 2.0 million to 3.0 million. Therefore, the current study has been conducted at a grid number of 2.0 million. The impeller passage is composed of approximately 1.3 million grids, and, the diffuser passage is composed of around 0.7 million grids.

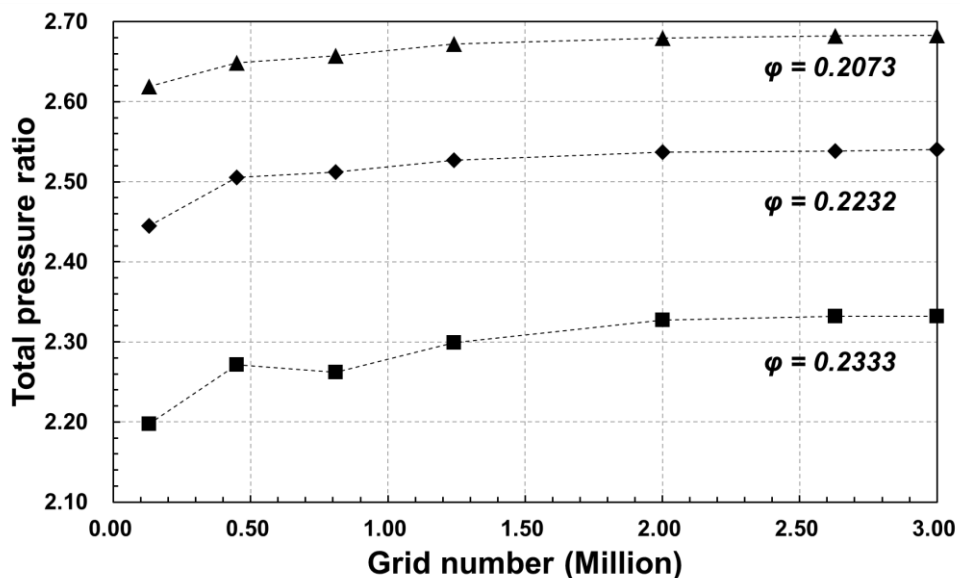


Figure 3.5. Grid dependence results.

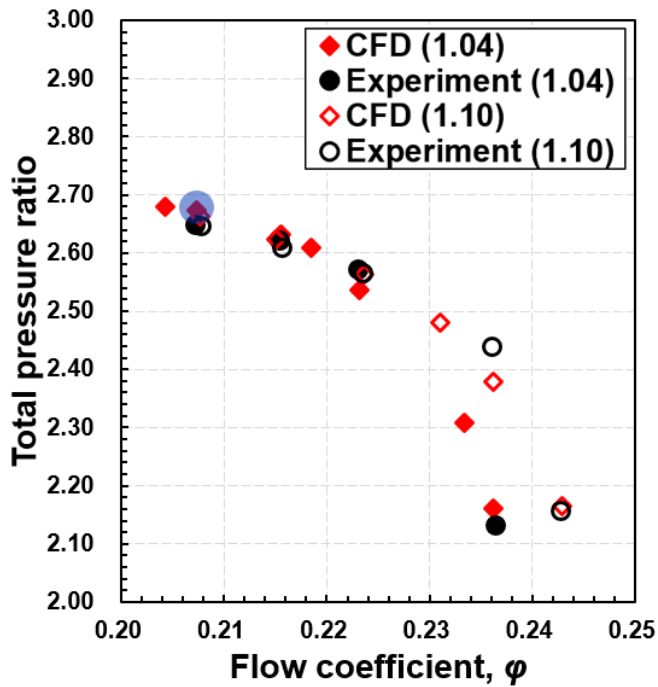
3.3.2. Compressor Map

To validate current numerical methods, steady simulation results have been compared against experimental data. Figures 3.6 (a) and (b) show comparisons of the predicted and measured total pressure ratios and isentropic efficiencies, respectively. Total pressure ratio and isentropic efficiency are defined in Eqs. (3.2) and (3.3), respectively. Results for the radial gap of 1.04 are marked with colored symbols and results for the radial gap of 1.10 are marked with uncolored symbols. For the radial gap of 1.04, predictions from the steady simulation match well with the experimental data to within 1.5%. For the radial gap of 1.10, predictions from the steady simulation match well with the experimental data to within 2.4%. In addition, variations of total pressure ratio and isentropic efficiency depending on the flow coefficient are well predicted regardless of the radial gap. Further validations have been conducted for the radial gap of 1.04 at the flow coefficient marked by blue circle in Fig. 3.6 (a).

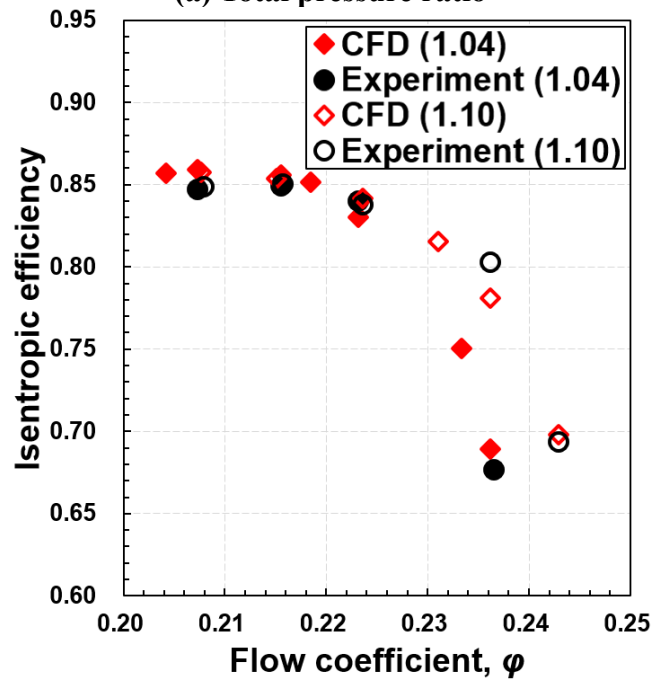
$$\pi_{tc} = \frac{\text{Mass averaged } P_t \text{ (Plane 8M)}}{P_t \text{ (Impeller inlet)}} \quad (3.2)$$

$$\eta_c = \frac{(\pi_{tc})^{\frac{\gamma-1}{\gamma}} - 1}{\tau_{tc} - 1} \quad (3.3)$$

$$\text{where } \tau_{tc} = \frac{\text{Mass averaged } T_t \text{ (Plane 8M)}}{T_t \text{ (Impeller inlet)}}$$



(a) Total pressure ratio

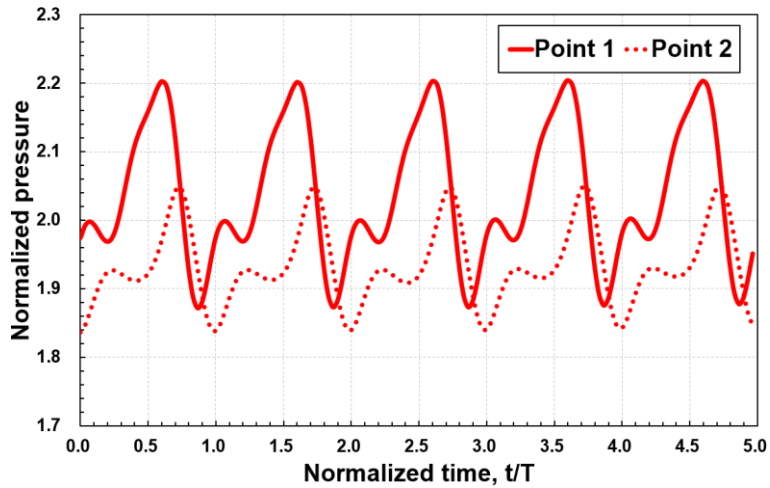


(b) Isentropic efficiency

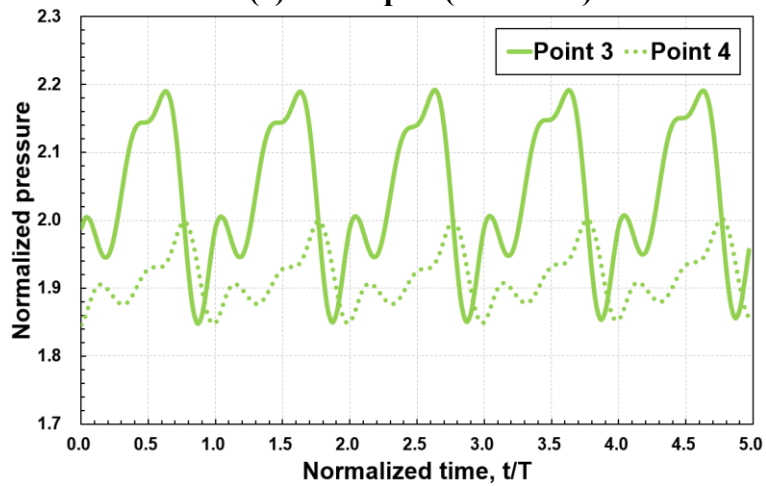
Figure 3.6. Comparison of compressor map – (a) total pressure ratio and (b) isentropic efficiency.

3.3.3. Periodicity of Unsteady Simulation

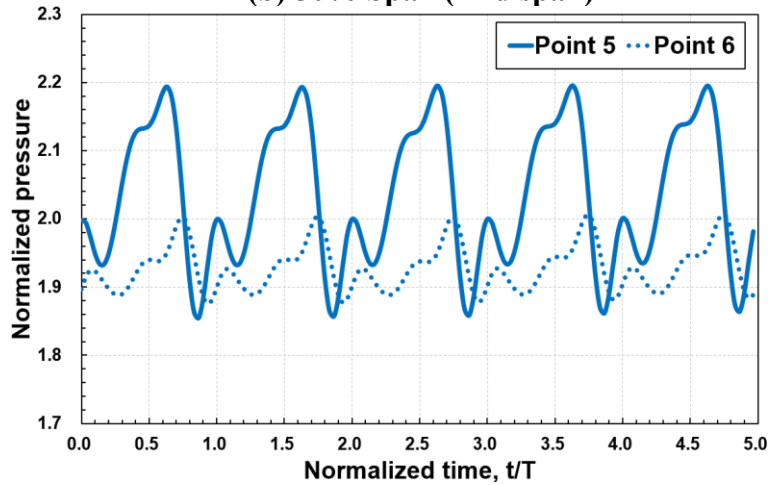
Before conducting a validation of the unsteady simulation, periodicities of pressure at six monitoring points (Table 3.1) for the radial gap of 1.04 and $\phi = 0.2073$ are shown in Figs. 3.7. Figures 3.7 (a), (b), and (c) show the periodicity results at 10% span, 50% span, and 90% span, respectively, for five diffuser vane passing periods. Static pressure has been normalized by dynamic pressure based on the impeller tip speed. At all six points, periodicity coefficients are below 0.5% and periodic solution has been obtained. Similar periodicities have also been confirmed for the every unsteady simulations.



(a) 10% Span (Near hub)



(b) 50% Span (Mid span)

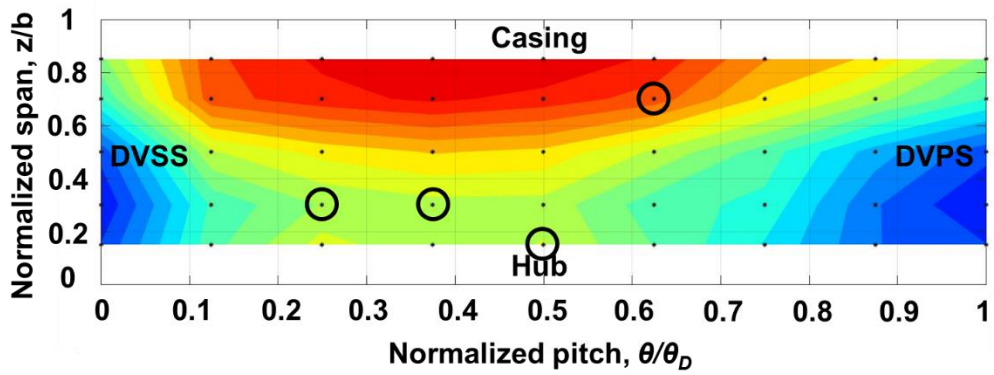


(c) 90% Span (Near shroud)

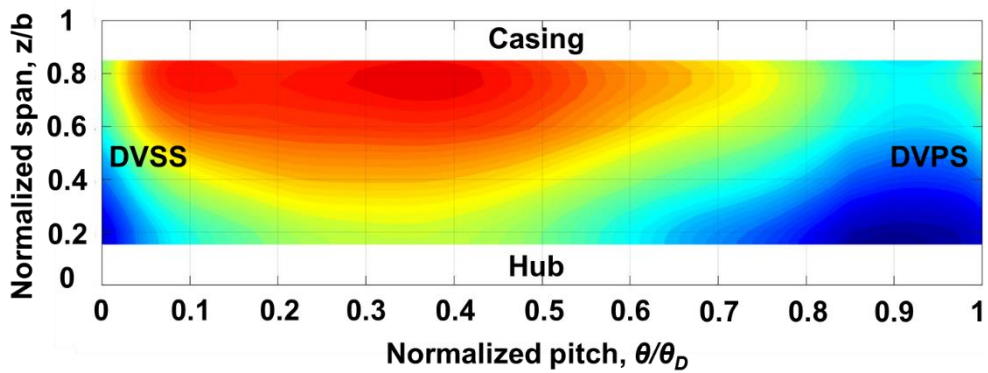
Figure 3.7. Pressure periodicities at six monitoring points.

3.3.4. Diffuser Vane Inlet Time Averaged Velocity Contour

Figures 3.8 (a) and (b) show time averaged absolute velocity contours from the experiment and unsteady simulation, respectively, at the diffuser vane inlet for the radial gap of 1.04 and $\varphi = 0.2073$ (Fig. 3.6 (a)). The vertical axis is the span-wise location and the horizontal axis is the pitch-wise location. Hub and casing correspond to $z/b = 0$ and 1, respectively, and, diffuser vane suction side (DVSS) and pressure side (DVPS) correspond to $\theta/\theta_D = 0$ and 1, respectively. Measurement locations are from the 4M plane in Fig. 2.2. Figure 3.8 (a) shows the measured velocity as well as the measurement locations (black dots) and 3.8 (b) the predicted velocity. The high-velocity region (near the diffuser vane suction side and the casing) and low velocity region (near the diffuser vane pressure side and the hub) are well simulated.



(a) Experiment



(b) Time average of unsteady simulation

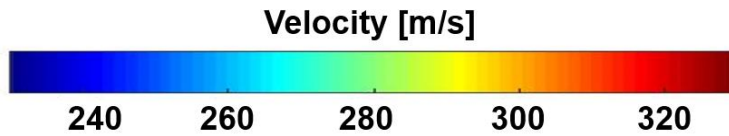


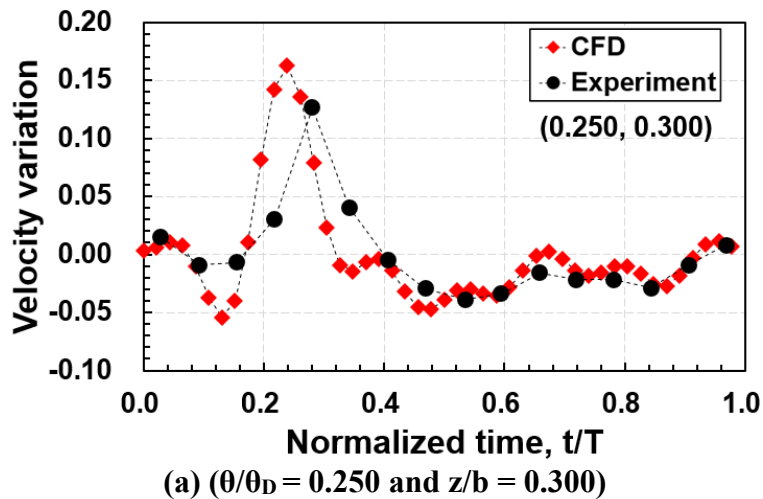
Figure 3.8. Diffuser vane inlet time averaged velocity contours - (a) measured and (b) predicted.

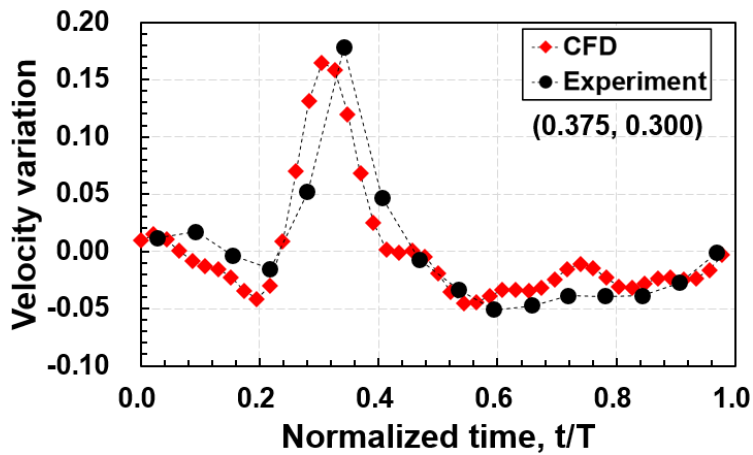
3.3.5. Diffuser Vane Inlet Temporal Velocity Variation

Figures 3.9 (a) to (d) show the measured and predicted velocity variations versus normalized time at four circled measurement points in Fig. 3.8 (a). Each measurement location has been indicated below each plot by normalized pitch-wise coordinate and normalized span-wise coordinate. Velocity variation is defined in Eq. (3.4) as the difference between the local instantaneous velocity and the local time averaged velocity normalized by the local time averaged velocity. At all four measurement points, temporal velocity variations are well predicted via unsteady simulation.

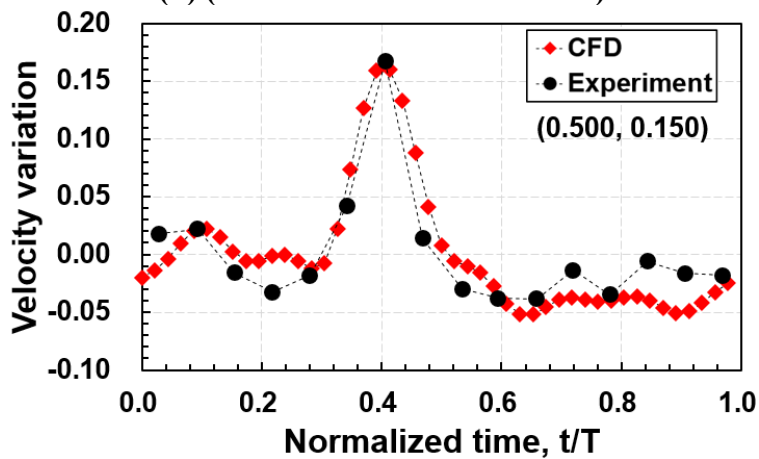
$$\begin{aligned} \text{Velocity variation} \\ = [C(\theta/\theta_D, z/b, t) - \bar{C}(\theta/\theta_D, z/b)] / \bar{C}(\theta/\theta_D, z/b) \end{aligned} \quad (3.4)$$

Lack of unsteady pressure data from “Radiver” prevents unsteady pressure comparison. Nevertheless, from the steady and unsteady velocity validations, the numerical methods can be judged to be reliable.

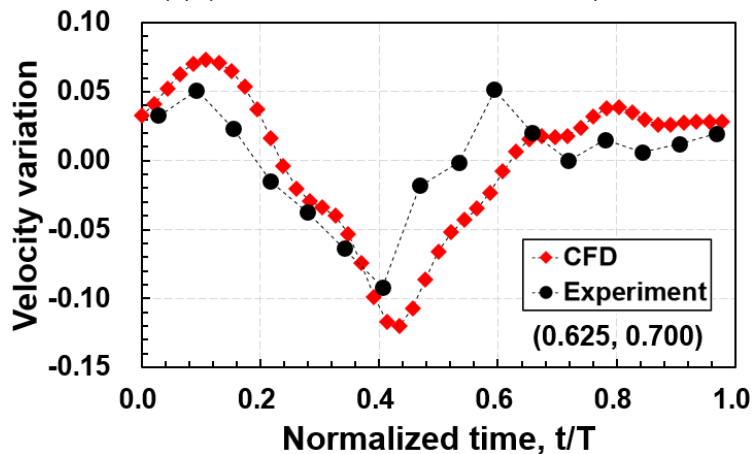




(b) ($\theta/\theta_D = 0.375$ and $z/b = 0.300$)



(c) ($\theta/\theta_D = 0.500$ and $z/b = 0.150$)



(d) ($\theta/\theta_D = 0.625$ and $z/b = 0.700$)

Figure 3.9. Diffuser vane inlet velocity variations with respect to time at four measurement points.

Chapter 4. Results and Discussions

4.1. Radial Gap of 1.04

4.1.1. Chord-wise Unsteady Loading Distribution

Figures 4.1 (a), (b), and (c) show the chord-wise distributions of unsteady loading per unit span at 10%, 50%, and 90% span-wise locations, respectively, for the radial gap of 1.04. Loading is defined in Eq. (4.1) as the static pressure difference between the impeller blade pressure and suction sides per unit span; and unsteady loading per unit span is defined in Eq. (4.2) as the difference between the maximum and the minimum loadings for a single diffuser passage period normalized by the dynamic pressure based on the impeller tip speed. At all span-wise locations, unsteady loading is the largest near the trailing edge and negligible for chord-wise coordinate locations less than 0.5. Furthermore, at all span-wise locations, the maximum unsteady loading is detected at around 0.98 chord-wise coordinate location; and the maximum unsteady loading is the largest at near stall, second largest at near choke, and smallest at the design condition. Table 4.1 summarizes the maximum unsteady loading at three flow coefficients and three span-wise locations. Maximum unsteady loading decreases from the hub to the shroud regardless of the flow coefficient. Similar span-wise variation has also been reported by Smythe [7] and Villanueva [8]. As distributions of the unsteady loading at three span-wise locations are qualitatively similar, further investigation has

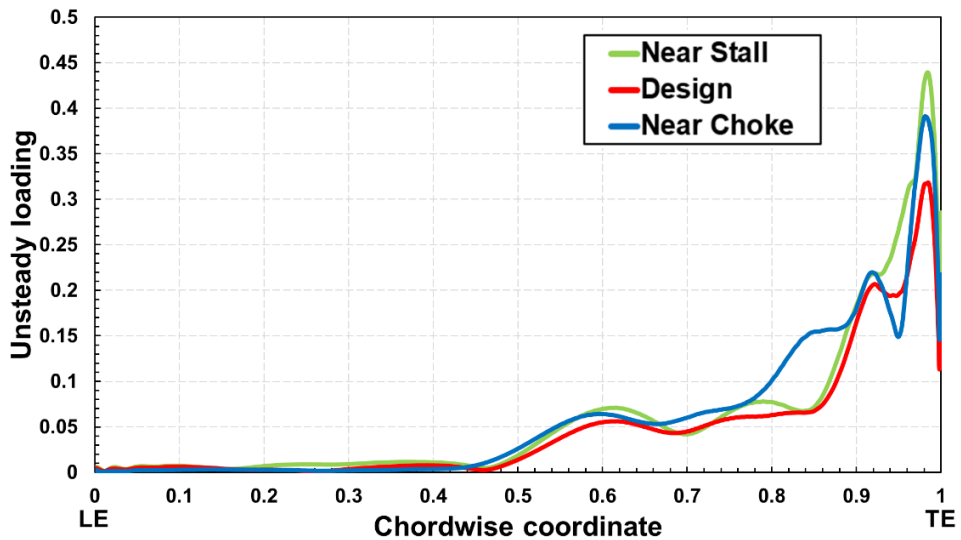
been conducted at 10% span-wise location (near the hub).

$$\text{Loading, } \Delta P = P_{PS} - P_{SS} \quad (4.1)$$

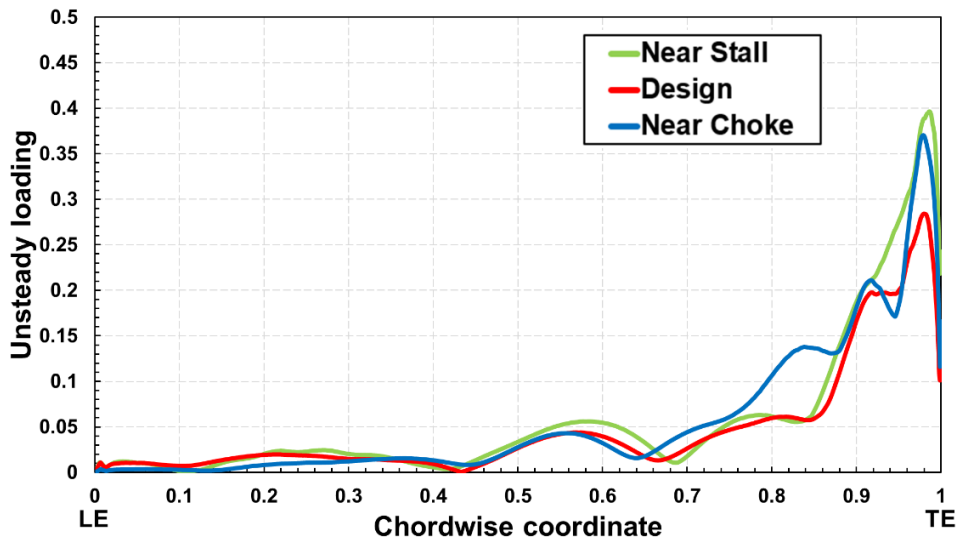
$$\text{Unsteady loading} = (\Delta P_{max} - \Delta P_{min}) / 0.5\rho U_{tip}^2 \quad (4.2)$$

Table 4.1 Maximum unsteady loading at three flow coefficients and three span-wise locations.

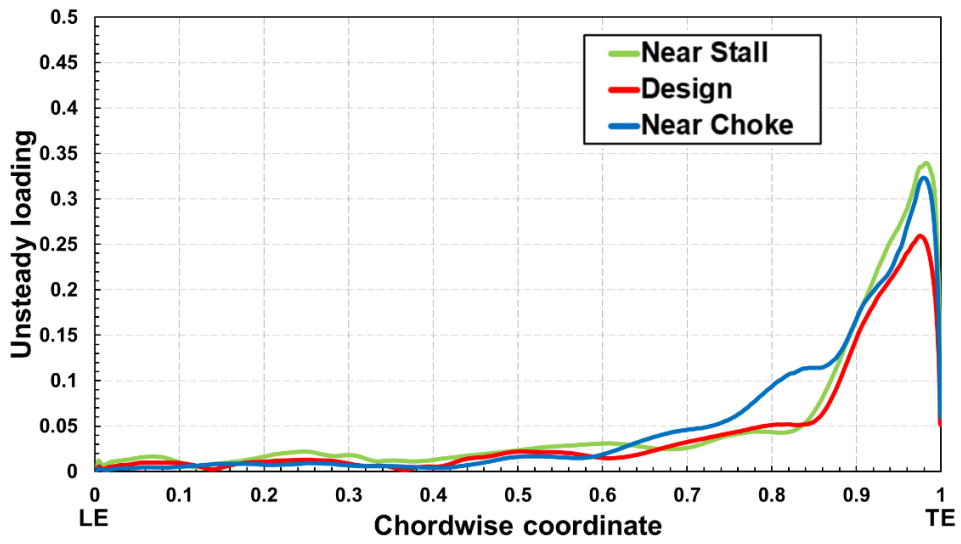
	Near stall	Design	Near choke
10% Span (near hub)	0.4394	0.3187	0.3914
50% Span (mid span)	0.3967	0.2842	0.3707
90% Span (near shroud)	0.3396	0.2593	0.3236



(a) 10% Span (Near hub)



(b) 50% Span (Mid span)



(c) 90% Span (Near shroud)

Figure 4.1. Chord-wise distributions of unsteady loading per unit span at (a) 10% span, (b) 50% span, and (c) 90% span.

4.1.2. Origin of Unsteady Loading

To examine the origin of the unsteady impeller loading, unsteady pressure at various instantaneous times has been investigated. Figures 4.2 (a) to (h) show normalized static pressure contours as well as chord-wise distributions of normalized loading fluctuation at the design condition and 10% span-wise location at various instantaneous times for the radial gap of 1.04. Static pressure has been normalized by the dynamic pressure based on the impeller tip speed and normalized loading fluctuation is defined in Eq. (4.3). Instantaneous time normalized by the diffuser vane passing period, T , has been denoted below each plot.

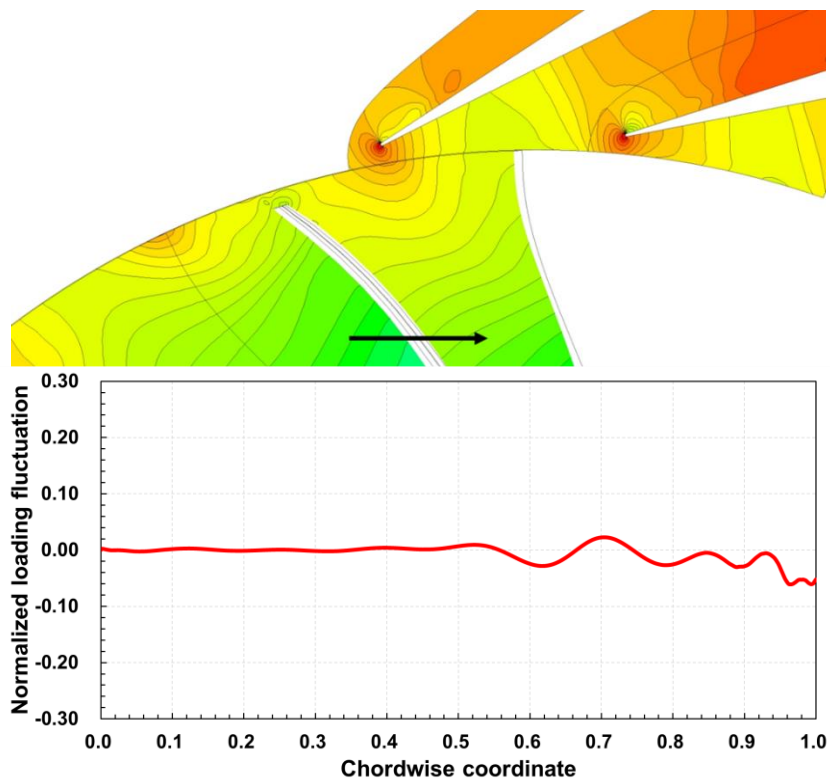
$$C_{\Delta P}(s, t)' = (\Delta P(s, t) - \overline{\Delta P(s)}) / 0.5\rho U_{tip}^2 \quad (4.3)$$

As the impeller rotates, the impeller blade pressure side approaches the diffuser vane leading edge stagnation pressure region. Thus, high pressure is imposed on the impeller blade pressure side, increasing blade loading near the trailing edge (Figs. 4.2 (a)-(d)). After the impeller blade rotates past the diffuser vane leading edge, pressure on the impeller blade pressure side is attenuated. Instead, the vane's stagnation pressure region increases pressure on the impeller blade suction side, decreasing blade loading near the trailing edge (Figs. 4.2 (e)-(f)). As the impeller blade approaches the middle of the diffuser vane passage, loading fluctuation approaches zero and impeller blade recovers the time-averaged blade loading (Figs. 4.2 (g)-(h)). Same

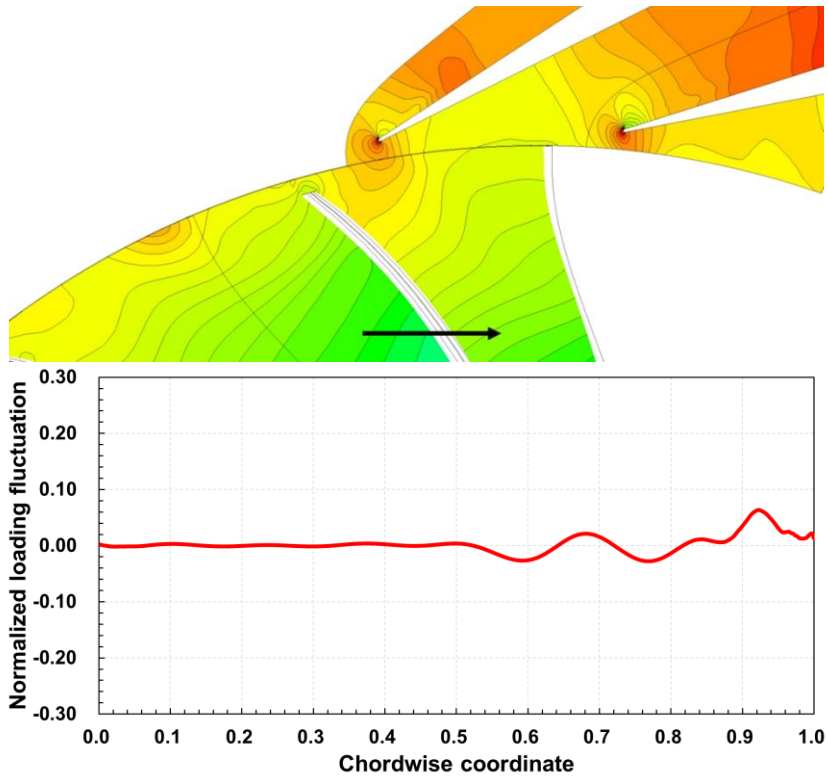
phenomenon repeats for every diffuser vane passage, resulting in a periodic unsteady loading on the impeller. Thus, physical mechanisms which drive the unsteady impeller loading induced by impeller-diffuser interaction can be summarized as follows:

1. Diffuser vane leading edge stagnation pressure imposes a high pressure on the impeller blade pressure side. Thus, blade loading increases.

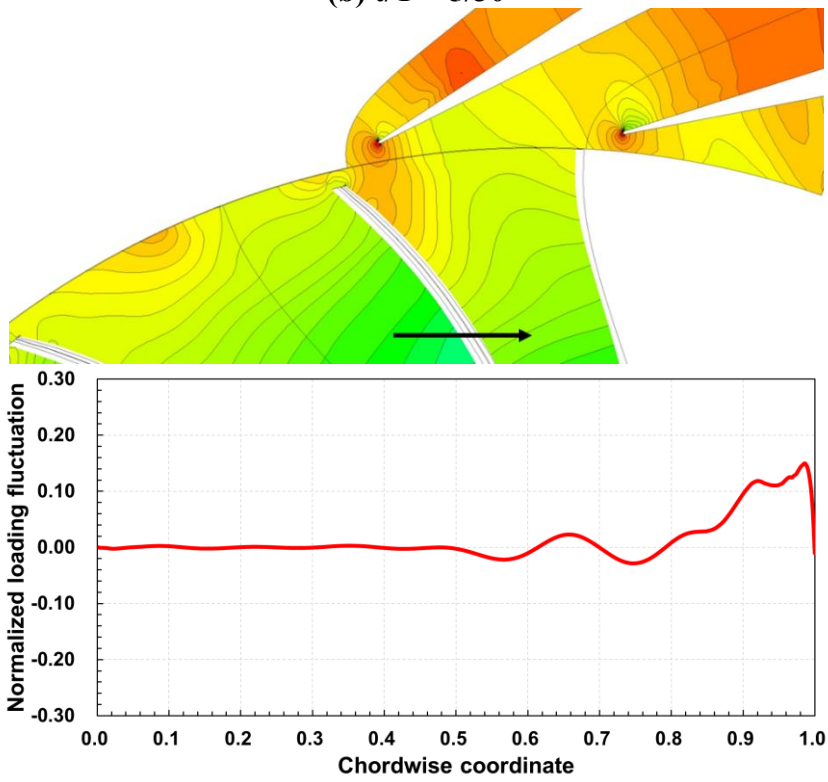
2. High pressure on the impeller blade pressure side is attenuated as the impeller blade rotates past the diffuser vane leading edge. Instead, the vane's stagnation pressure region increases pressure on the impeller blade suction side. Thus, blade loading decreases.



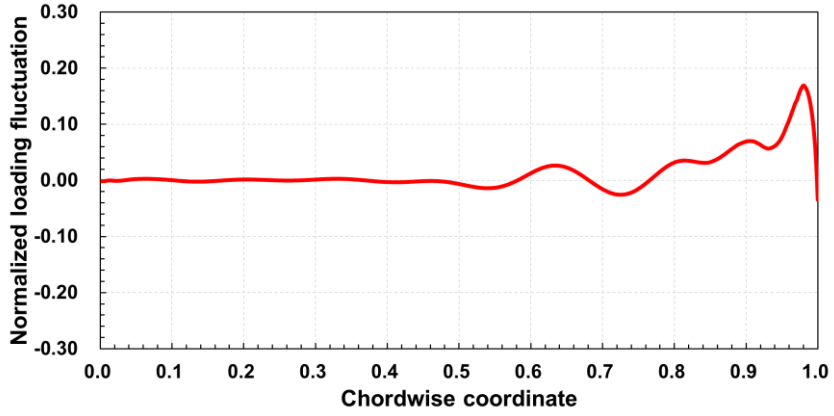
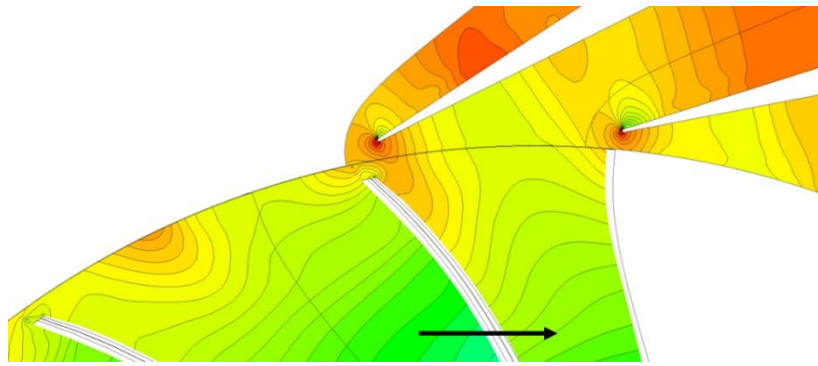
(a) $t/T = 1/30$



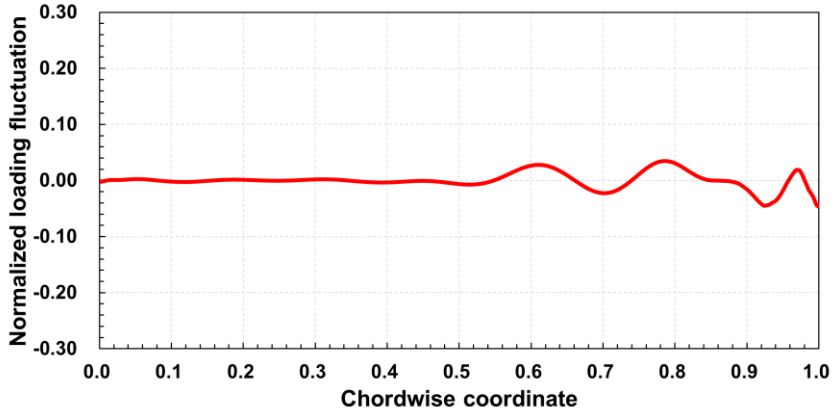
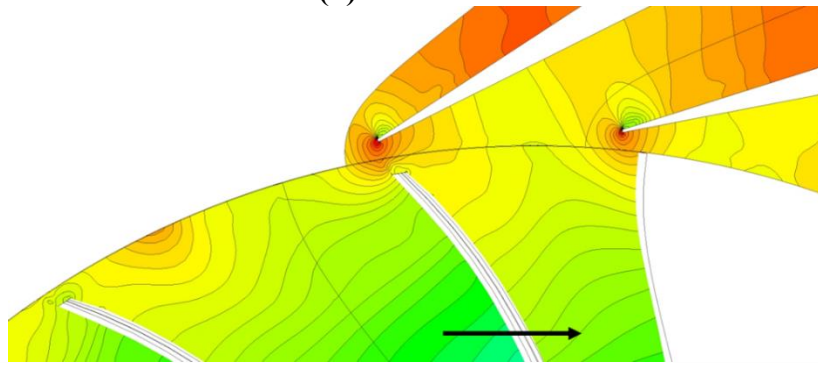
(b) $t/T = 5/30$



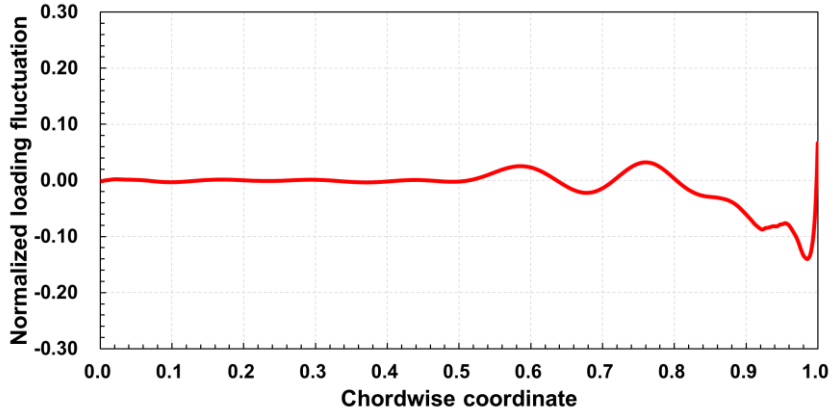
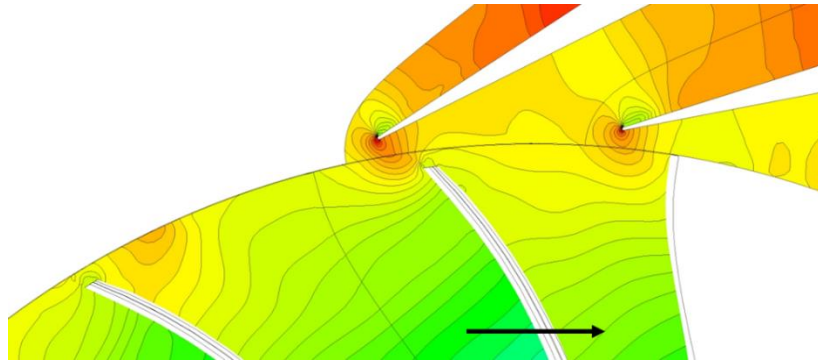
(c) $t/T = 9/30$



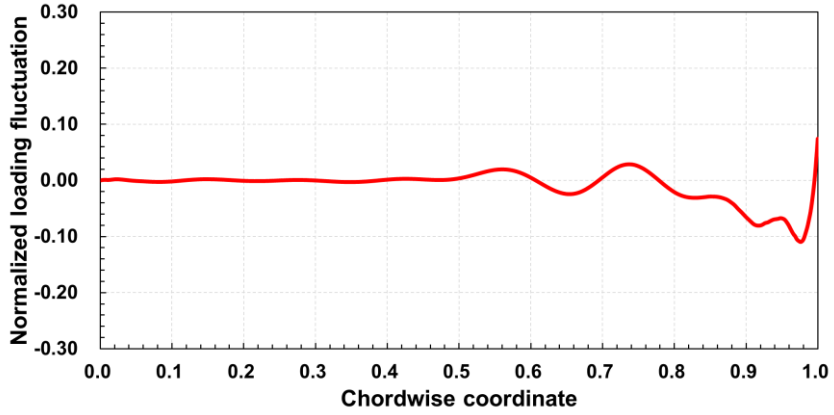
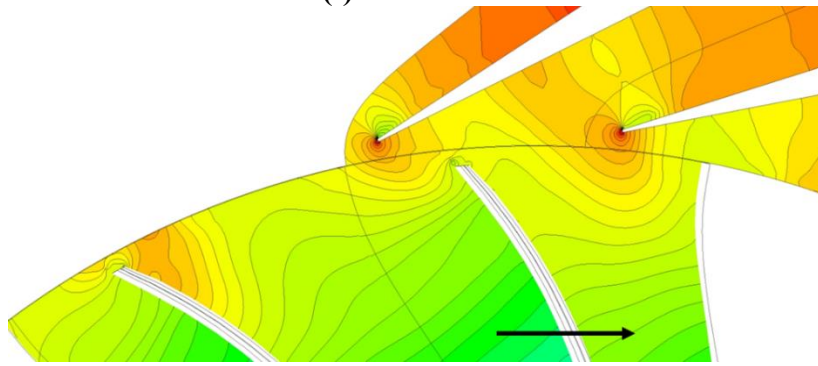
(d) $t/T = 13/30$



(e) $t/T = 17/30$



(f) $t/T = 21/30$



(g) $t/T = 25/30$

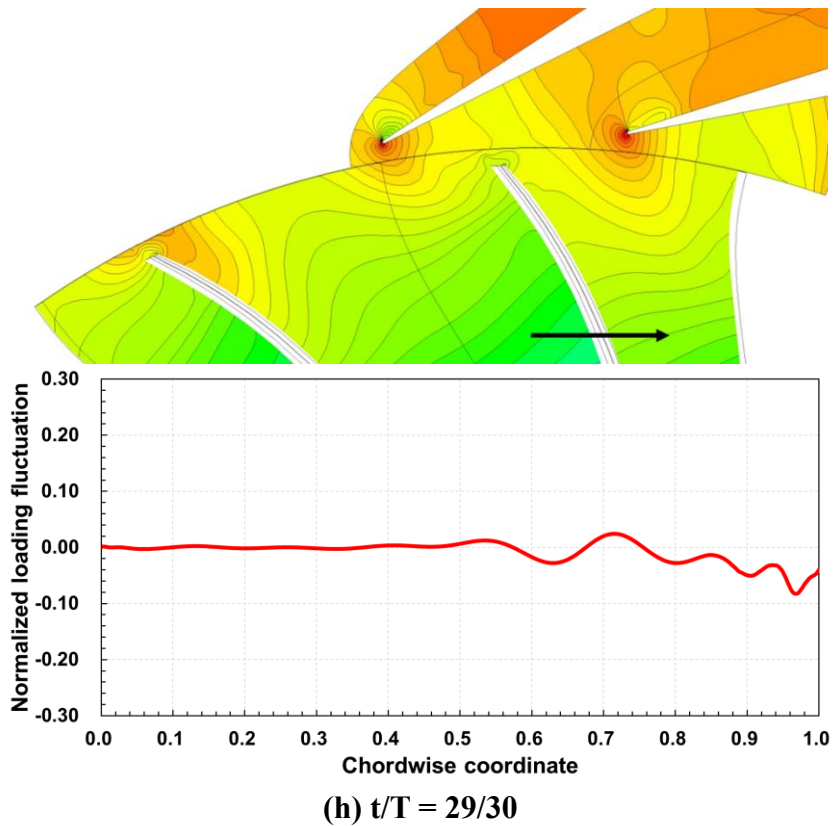


Figure 4.2. Normalized static pressure contours and loading fluctuations at the design condition and 10% span-wise location.

4.1.3. Fast Fourier Transformation Analysis

To determine the frequency contents of the unsteady loading, Fast Fourier Transformation (FFT) analysis has been conducted. Figure 4.3 shows the FFT results of the unsteady loading at 0.98 chord-wise coordinate location (where the maximum unsteady loading has been detected) for three flow coefficients. Frequency has been normalized by the diffuser vane passing frequency and the magnitude has been normalized by the maximum magnitude. The first harmonic is dominant and the second harmonic decreases by around a factor of two regardless of the flow coefficient. In addition, higher harmonics are negligible compared to the first harmonic. Thus, the dominant frequency of the unsteady loading corresponds to the diffuser vane passing frequency regardless of the flow coefficient.

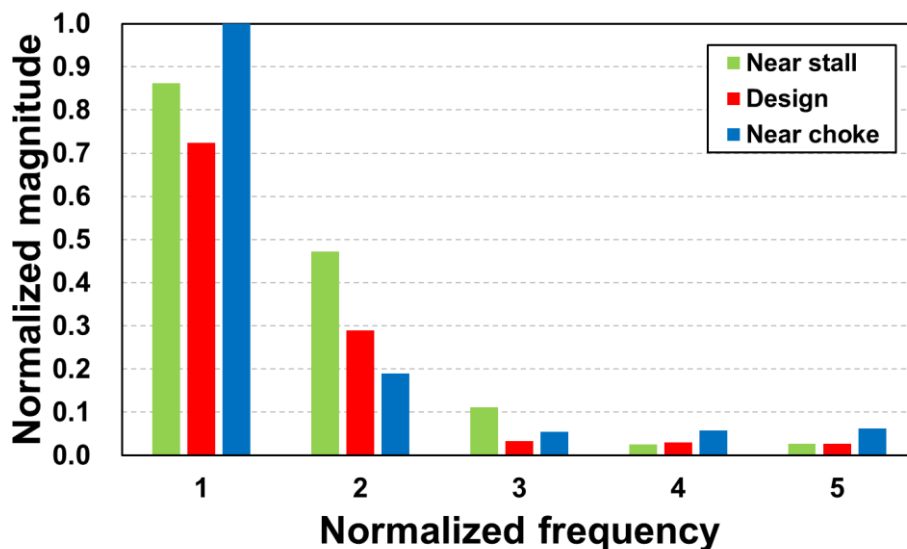


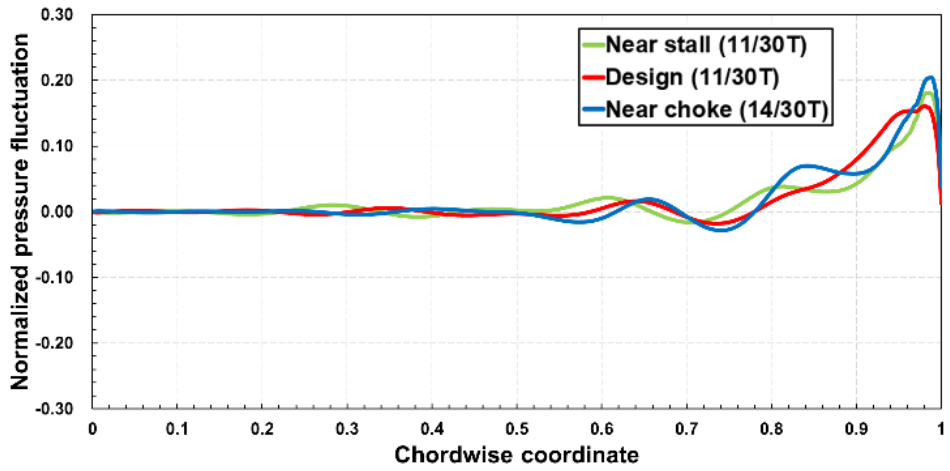
Figure 4.3. Frequency contents of the unsteady loading at 0.98 chord-wise coordinate location.

4.1.4. Loading and Pressure Fluctuations

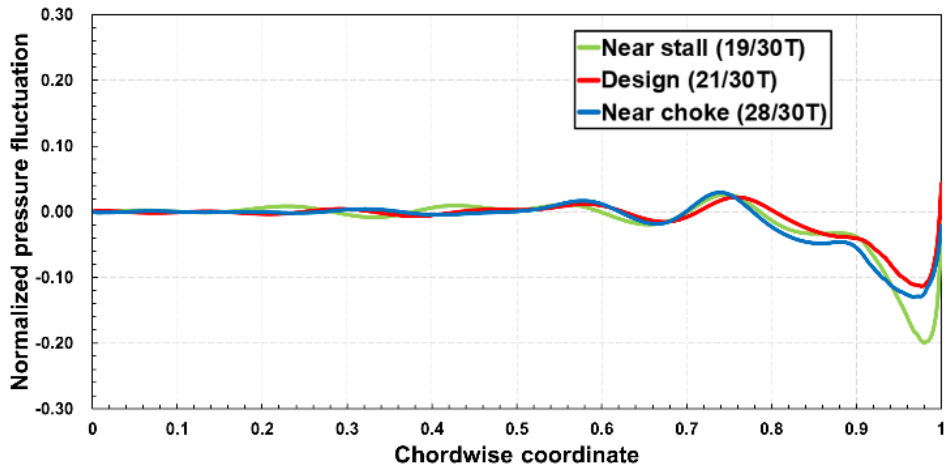
To further elucidate the influence of flow coefficient on the unsteady loading, the former's effects on the maximum and the minimum loadings have been investigated. Figures 4.4 (a) to (f) show the chord-wise distributions of pressure side pressure fluctuations for maximum and minimum loadings (Figs. 4.4. (a) and (b)), corresponding suction side pressure fluctuations (Figs. 4.4. (c) and (d)), and corresponding loading fluctuations (Figs. 4.4. (e) and (f)) at three flow coefficients (near stall, design, and near choke conditions) for the radial gap of 1.04. Normalized pressure fluctuations on the pressure and the suction sides are defined in Eqs. (4.4) and (4.5), respectively.

$$C_{P,PS}(s, t)' = (P_{PS}(s, t) - \overline{P_{PS}(s)}) / 0.5\rho U_{tip}^2 \quad (4.4)$$

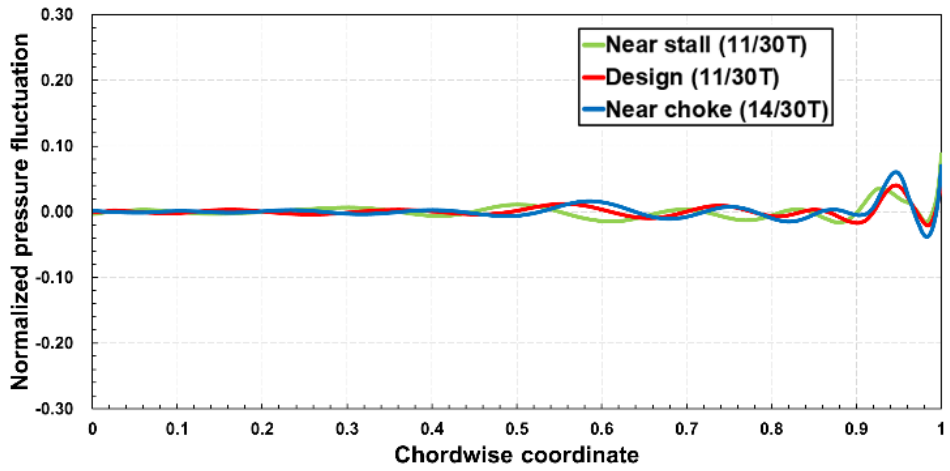
$$C_{P,SS}(s, t)' = (P_{SS}(s, t) - \overline{P_{SS}(s)}) / 0.5\rho U_{tip}^2 \quad (4.5)$$



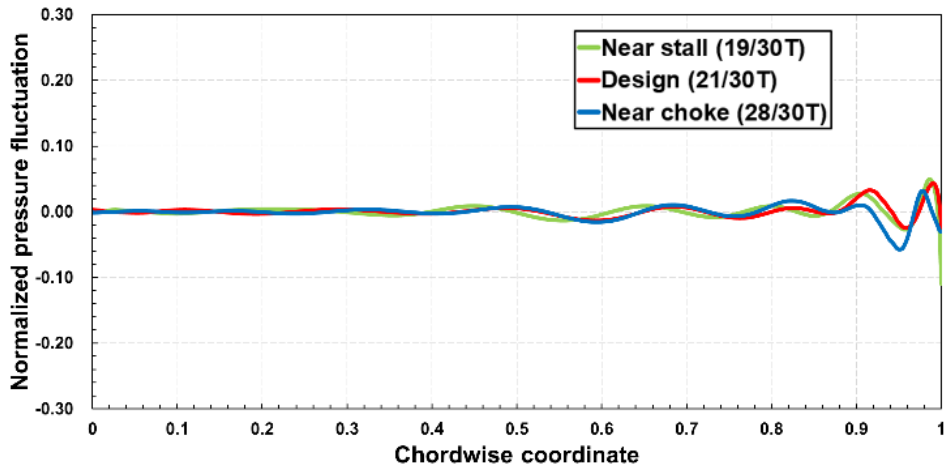
(a) Pressure side pressure fluctuations at maximum loading



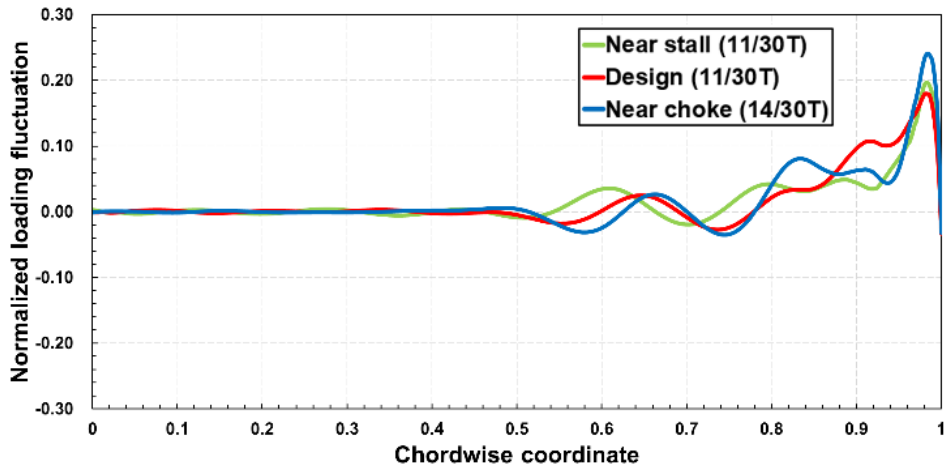
(b) Pressure side pressure fluctuations at minimum loading



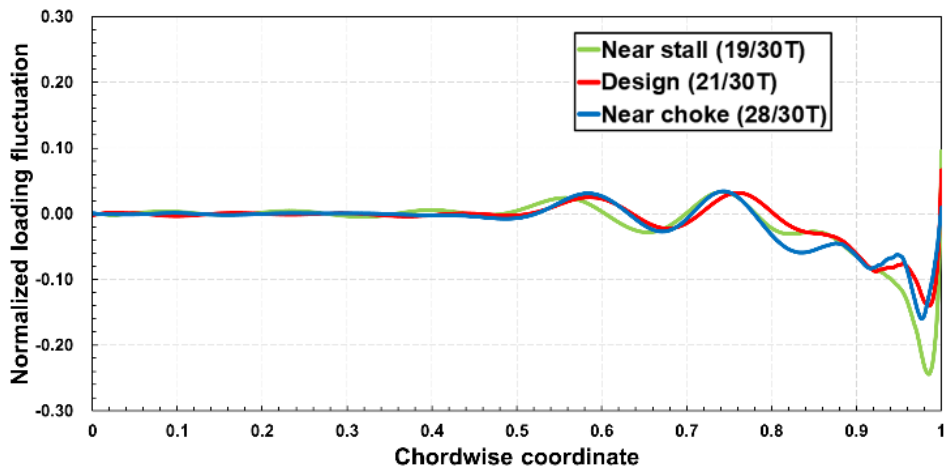
(c) Suction side pressure fluctuations at maximum loading



(d) Suction side pressure fluctuations at minimum loading



(e) Loading fluctuations at maximum loading



(f) Loading fluctuations at minimum loading

Figure 4.4. Chord-wise distributions of (a)-(b) pressure side pressure fluctuations, (c)-(d) suction side pressure fluctuations, and (e)-(f) loading fluctuations at near stall, design, and near choke conditions.

For the near stall condition maximum loading, the maximum pressure on the pressure side is similar to that at the design condition (Fig. 4.4 (a)). However, at the minimum loading, the minimum pressure on the pressure side is lower than at the design condition (Fig. 4.4 (b)). No such dependence on the flow coefficient is visible on the suction side (Figs. 4.4 (c) and (d)). Thus, flow coefficient mainly affects pressure on the pressure side, and loading displays similar trends. Consequently, as unsteady loading is determined by the difference between the maximum and the minimum loadings, near stall condition has higher unsteady loading than the design condition.

On the other hand, the near choke condition has a higher maximum pressure on the pressure side than the design condition at the maximum loading (Fig. 4.4 (a)). At the minimum loading, the near choke condition has a similar minimum pressure on the pressure side as the design condition (Fig. 4.4 (b)). Again, such dependence on the flow coefficient is weak on the suction side (Figs. 4.4 (c) and (d)). Therefore, the near choke condition has a higher unsteady loading than the design condition.

4.1.5. Diffuser Vane Inlet Pressure Distribution

To investigate how the flow coefficient affects pressure fluctuations on the impeller blade pressure side, pitch-wise pressure distribution at the diffuser vane inlet has been examined. Figure 4.5 shows the pitch-wise time averaged non-dimensional static pressure distributions at $r/r_2 = 1.039$ for three flow coefficients. $\theta/\theta_D = 0$ corresponds to the diffuser vane leading edge. At the near stall condition, pressure near the diffuser vane leading edge is similar to that of the design condition. Since the maximum loading is set by the high pressure near the diffuser vane leading edge, the maximum loadings of two conditions are similar (Fig. 4.4 (e)). However, compared to the design condition, pressure drops more rapidly after the impeller blade passes by the diffuser vane leading edge at the near stall condition. Thus, the high pressure imposed on the impeller blade pressure side decays more rapidly and results in a lower minimum loading (Fig. 4.4 (f)).

Conversely, relative to the design condition, pressure near the diffuser vane leading edge is higher at the near choke condition. Thus, higher pressure is imposed on the impeller blade pressure side, resulting in a higher maximum loading (Fig. 4.4 (e)). After the impeller blade passing by the diffuser vane leading edge, pressure decreases in the pitch-wise direction are similar at both the design and near choke conditions, leading to similar minimum loadings (Fig. 4.4 (f)).

Villanueva [8] suggested that the “difference in static pressure from the pressure surface to the suction surface at the leading edge of the diffuser vane”

sets the unsteady loading. However, the current study suggests that, in addition, the pitch-wise static pressure distribution near the diffuser vane leading edge influences the unsteady impeller loading.

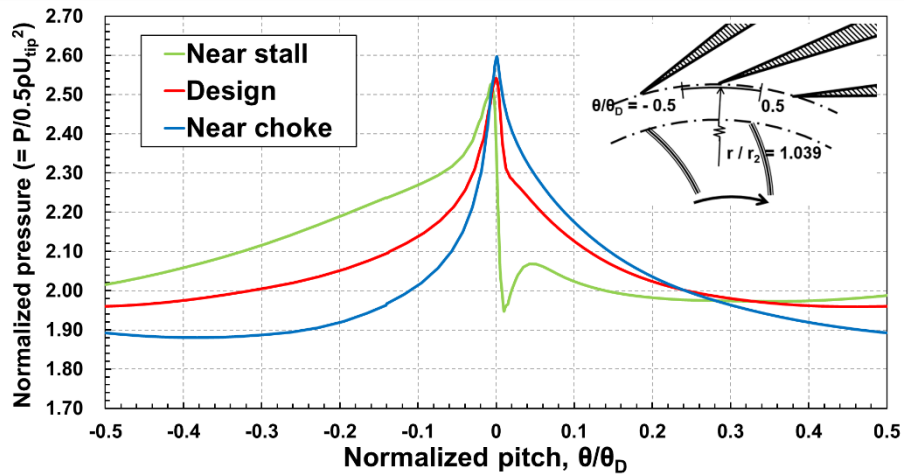
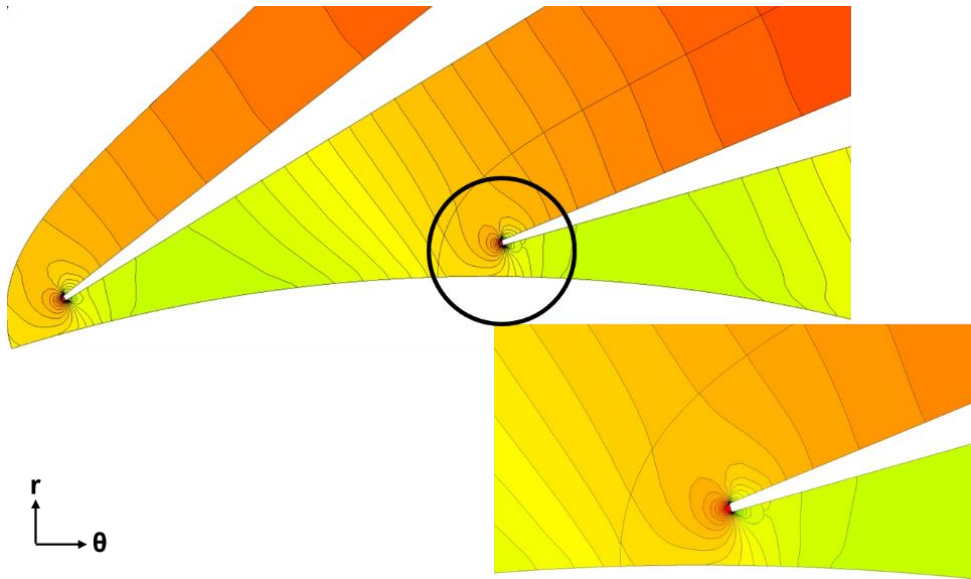
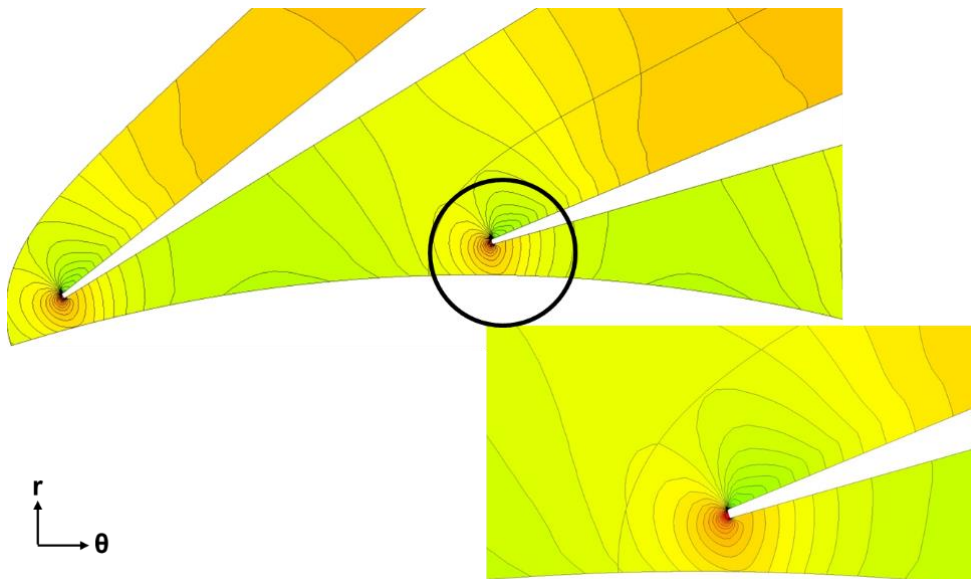


Figure 4.5. Pitch-wise time averaged static pressure distributions at $r/r_2 = 1.039$.

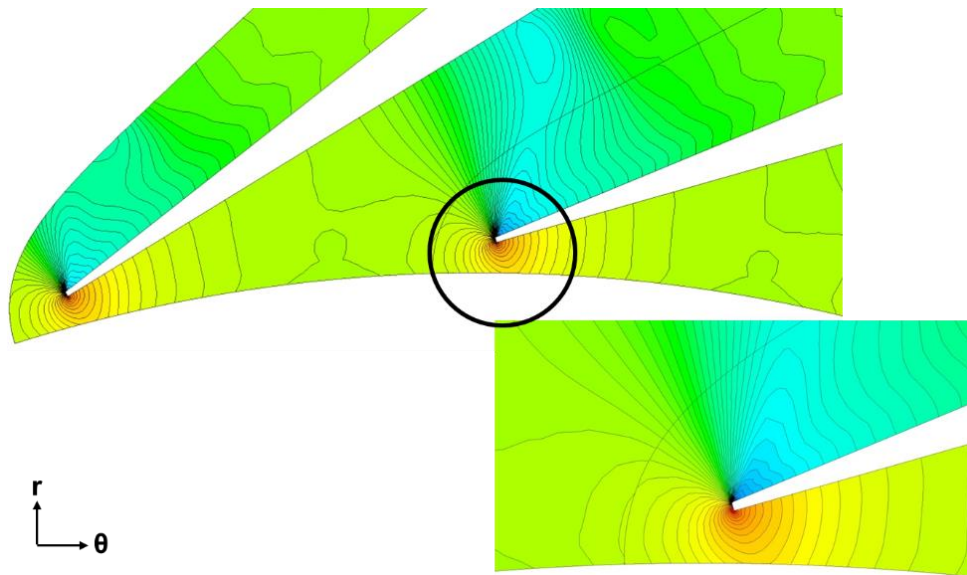
Variations in the pitch-wise pressure distributions in Fig. 4.5 are set by the diffuser vane inlet pressure fields. Therefore, Figs. 4.6 (a) to (c) show the non-dimensional time averaged diffuser vane inlet pressure fields at near stall (Fig. 4.6 (a)), design (Fig. 4.6 (b)), and near choke (Fig. 4.6 (c)) conditions. Pressure contour near the diffuser vane leading edge is symmetric about the diffuser vane center line at the near stall condition. However, as the flow coefficient increases, the stagnation point moves increasingly toward the suction side of the diffuser vane leading edge and the pressure field becomes asymmetric. Liu et al. [15] reported a similar trend. Such differences stem from decreasing incidence as flow coefficient increases. Diffuser vane incidence is defined as the difference between the flow angle and the diffuser vane center line angle at the vane inlet. Incidence has been taken as positive when its direction is identical to impeller rotating direction (Fig. 4.7). As the flow coefficient increases, incidence decreases and the impeller exit absolute velocity becomes more radial (Fig. 4.7), altering the diffuser vanes' potential field and pitch-wise pressure distribution.



(a) Near stall



(b) Design



(c) Near choke

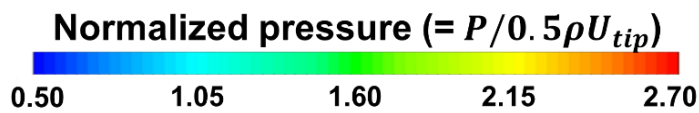


Figure 4.6. Time averaged diffuser vane inlet pressure fields at (a) near stall, (b) design, and (c) near choke conditions.

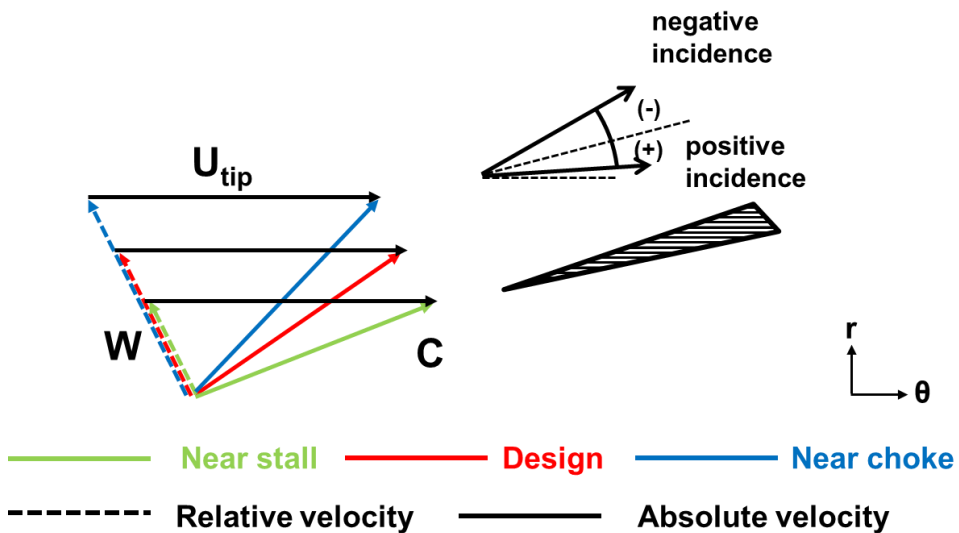
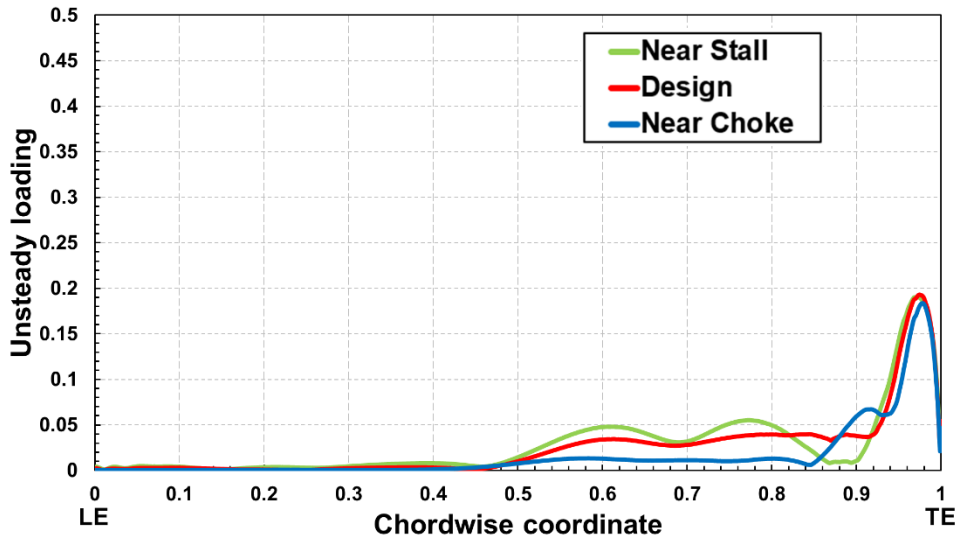


Figure 4.7. Velocity triangles of impeller exit flow at three flow coefficients.

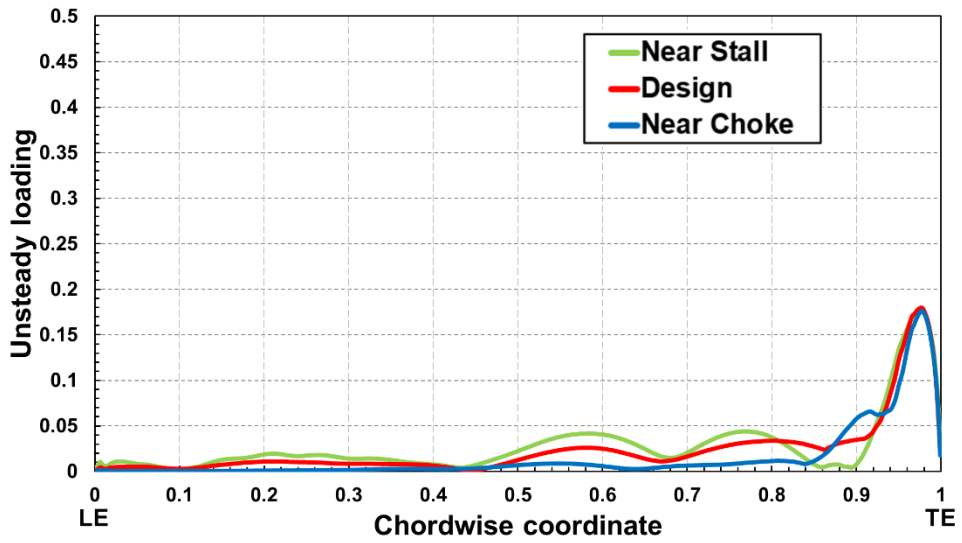
4.2. Radial Gap of 1.10

4.2.1. Chord-wise Unsteady Loading Distribution

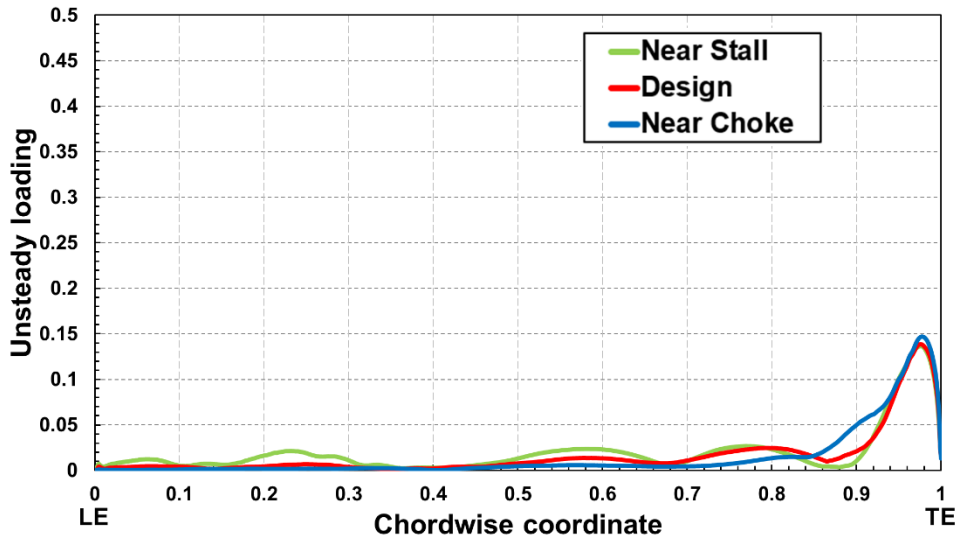
Figures 4.8 (a), (b), and (c) show the chord-wise distributions of unsteady loading per unit span at 10%, 50%, and 90% span-wise locations, respectively, for the radial gap of 1.10. At all span-wise locations, unsteady loading is the largest near the trailing edge and negligible for chord-wise coordinate locations less than 0.5. Furthermore, at all span-wise locations, the maximum unsteady loading is detected at around 0.98 chord-wise coordinate location. However, unlike the results for the radial gap of 1.04, flow coefficient has negligible effects on the unsteady loading. Table 4.2 summarizes the maximum unsteady loading at three flow coefficients and three span-wise locations. Maximum unsteady loading decreases from the hub to the shroud regardless of the flow coefficient. However, effects of flow coefficient are invisible. As distributions of the unsteady loading at three span-wise locations are qualitatively similar, further investigation has been conducted at 10% span-wise location (near the hub).



(a) 10% Span (Near hub)



(b) 50% Span (Mid span)



(c) 90% Span (Near shroud)

Figure 4.8. Chord-wise distributions of unsteady loading per unit span at (a) 10% span, (b) 50% span, and (c) 90% span.

Table 4.2 Maximum unsteady loading at three flow coefficients and three span-wise locations.

	Near stall	Design	Near choke
10% Span (near hub)	0.1907	0.1933	0.1837
50% Span (mid span)	0.1759	0.1798	0.1764
90% Span (near shroud)	0.1367	0.1389	0.1470

4.2.2. Fast Fourier Transformation Analysis

To determine the frequency contents of the unsteady loading, Fast Fourier Transformation (FFT) analysis has been conducted. Figure 4.9 shows the FFT results of the unsteady loading at 0.98 chord-wise coordinate location (where the maximum unsteady loading has been detected) for three flow coefficients. Frequency has been normalized by the diffuser vane passing frequency and the magnitude has been normalized by the maximum magnitude. The first harmonic is dominant and the second harmonic decreases by around a factor of five regardless of the flow coefficient. In addition, higher harmonics are negligible compared to the first harmonic. Thus, the dominant frequency of the unsteady loading corresponds to the diffuser vane passing frequency regardless of the flow coefficient.

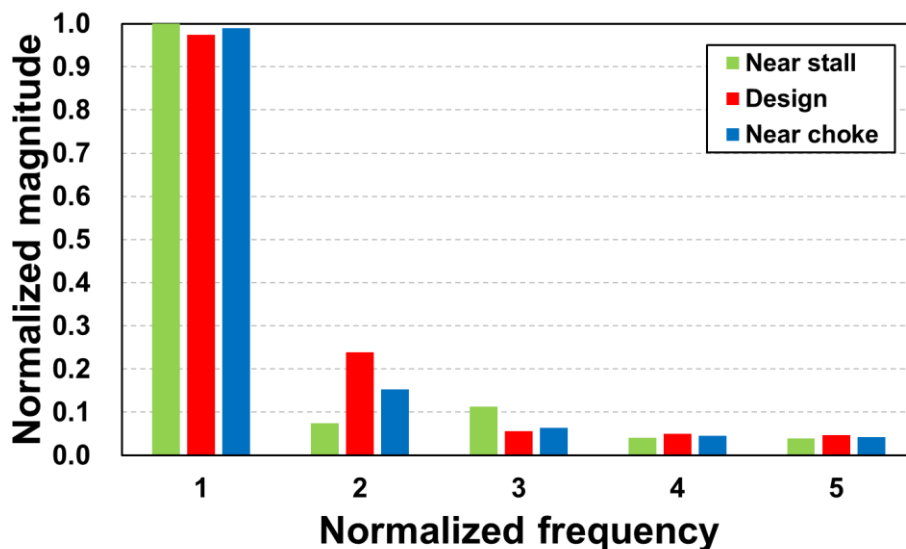
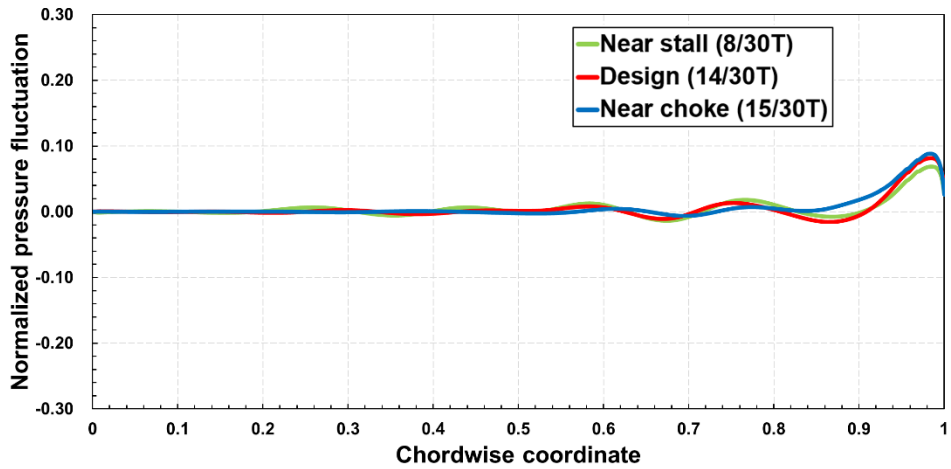


Figure 4.9. Frequency contents of the unsteady loading at 0.98 chord-wise coordinate location.

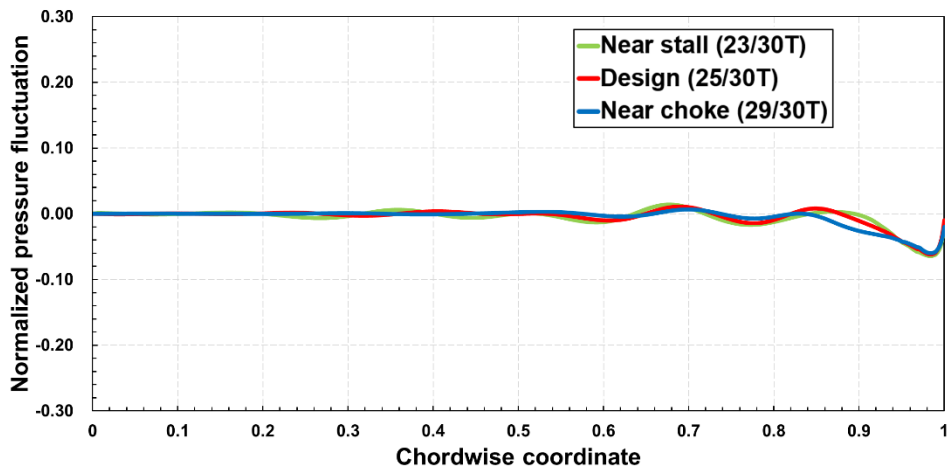
4.2.3. Loading and Pressure Fluctuations

To further elucidate why the flow coefficient has a negligible influence on the unsteady loading, the former's effects on the maximum and the minimum loadings have been investigated. Figures 4.10 (a) to (f) show the chord-wise distributions of pressure side pressure fluctuations for maximum and minimum loadings (Figs. 4.10. (a) and (b)), corresponding suction side pressure fluctuations (Figs. 4.10. (c) and (d)), and corresponding loading fluctuations (Figs. 4.10. (e) and (f)) at three flow coefficients (near stall, design, and near choke conditions) for the radial gap of 1.10. Normalized pressure fluctuations on the pressure and the suction sides are defined in Eqs. (4.4) and (4.5), respectively.

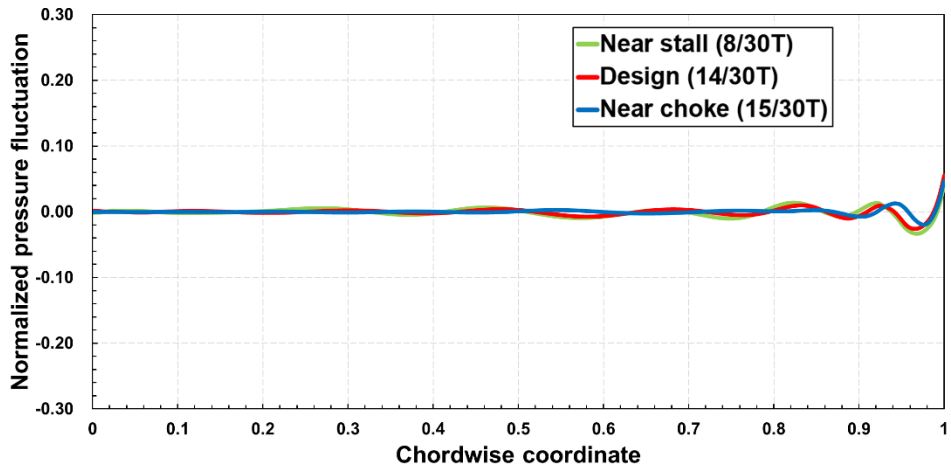
Unlike the results for the radial gap of 1.04, flow coefficient has negligible effects on the pressure on the pressure side at both maximum and minimum loadings. Again, such dependence on the flow coefficient is invisible on the suction side, and, thus, loading displays similar trends as that of the pressure fluctuation on the pressure side.



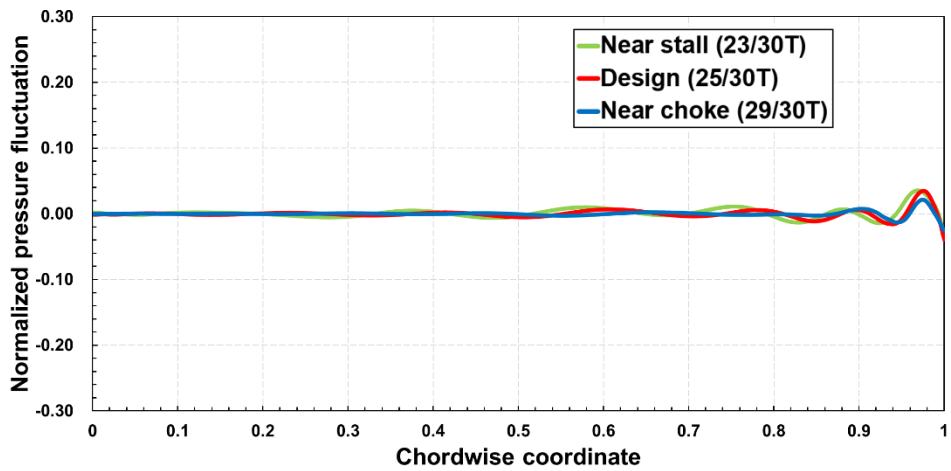
(a) Pressure side pressure fluctuations at maximum loading



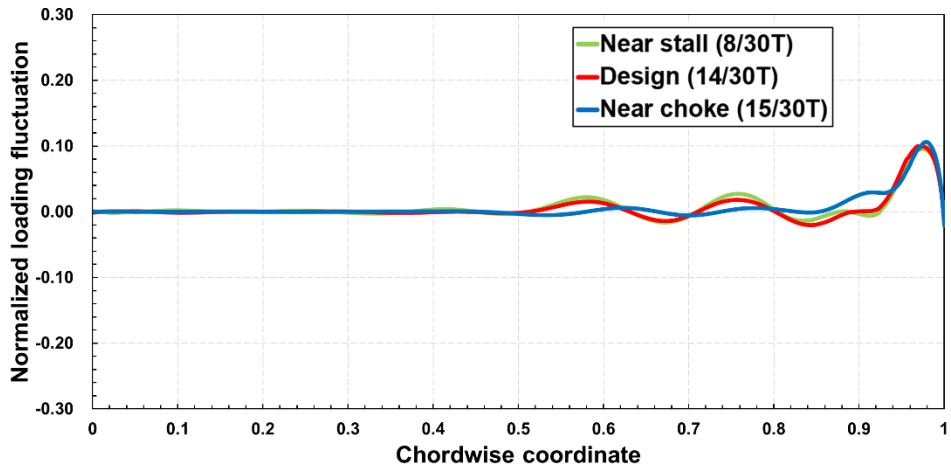
(b) Pressure side pressure fluctuations at minimum loading



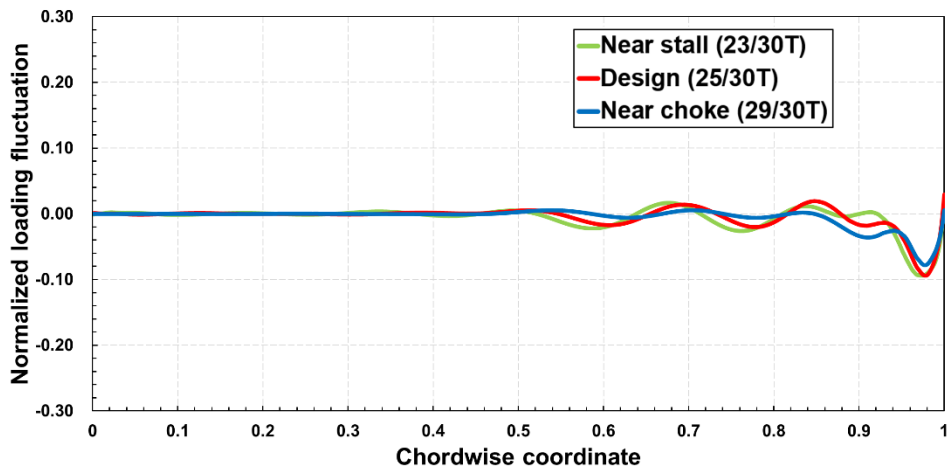
(c) Suction side pressure fluctuations at maximum loading



(d) Suction side pressure fluctuations at minimum loading



(e) Loading fluctuations at maximum loading



(f) Loading fluctuations at minimum loading

Figure 4.10. Chord-wise distributions of (a)-(b) pressure side pressure fluctuations, (c)-(d) suction side pressure fluctuations, and (e)-(f) loading fluctuations at near stall, design, and near choke conditions.

4.2.4. Diffuser Vane Inlet Pressure Distribution

Pitch-wise pressure distribution at the diffuser vane inlet has been examined as for the radial gap of 1.04. Figure 4.11 shows the pitch-wise time averaged non-dimensional static pressure distributions at $r/r_2 = 1.099$ for three flow coefficients. $\theta/\theta_D = 0$ corresponds to the diffuser vane leading edge. At the near stall condition, pressure near the diffuser vane leading edge is lower than that of the design condition. Furthermore, pressure drops more rapidly after the impeller blade passes by the diffuser vane leading edge at the near stall condition. However, unlike the results for the radial gap of 1.04, influence of flow coefficient on the maximum and the minimum loadings is invisible.

Conversely, relative to the design condition, pressure near the diffuser vane leading edge is higher and pressure drops less rapidly after the diffuser vane leading edge at the near choke condition. However, like the results at the near stall condition, influence of flow coefficient on the maximum and the minimum loadings is invisible.

Thus, as described in Fig. 4.12, flow coefficient affects the pitch-wise pressure distribution and the potential field at the diffuser vane. However, as the radial gap increases, the potential effect of the diffuser vane is attenuated, and, thus, the influences of flow coefficient on the pressure fluctuations on the impeller blade pressure side and the unsteady impeller loading are negligible.

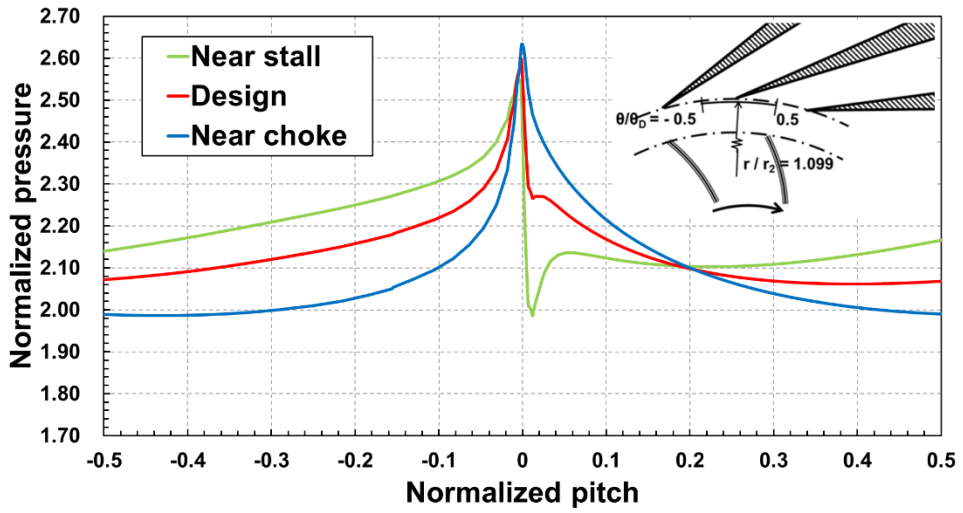


Figure 4.11. Pitch-wise time averaged static pressure distributions at $r/r_2 = 1.099$.

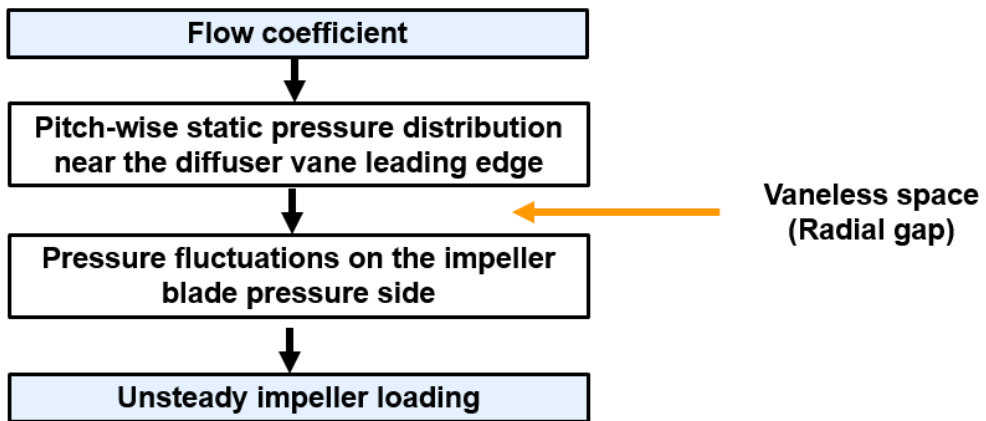


Figure 4.12. Schematic of the influence of flow coefficient on the unsteady impeller loading.

Chapter 5. Conclusions

The objective of the current study is to numerically investigate the influence of flow coefficient on the unsteady impeller loading at two radial gaps in a high-speed compressor. Conclusions from this study are as follows:

1. For the radial gap of 1.04, the unsteady loading is the largest at the near stall condition; second largest at the near choke condition; and smallest at the design condition.

2. Pressure fluctuations on the pressure side is mostly responsible for the dependence of unsteady impeller loading on the flow coefficient.

3. At the near stall condition, high pressure imposed on the impeller blade pressure side decays more rapidly than at the design condition. Thus, near stall condition has a lower minimum loading and a higher unsteady loading than at the design condition.

4. At the near choke condition, higher pressure is imposed on the impeller blade pressure side than at the design condition. Consequently, the near choke condition has a higher maximum loading and a higher unsteady loading than at the design condition.

5. Such variations stem from pitch-wise static pressure distribution and the potential field at the diffuser vane inlet which are determined by the diffuser vane incidence.

6. For the radial gap of 1.10, the influence of flow coefficient on the unsteady loading is negligible.

7. Such independence stems from the attenuated potential effect of the diffuser vane as the radial gap increases.

Bibliography

- [1] Ziegler, K. U., Gallus, H. E., and Niehuis, R., 2003. "A study on impeller-diffuser interaction. Part I: Influence on the performance". *Journal of Turbomachinery*, **125**(1), pp. 173-182.
- [2] Ziegler, K. U., Gallus, H. E., and Niehuis, R., 2003. "A study on impeller-diffuser interaction. Part II: Detailed flow analysis". *Journal of Turbomachinery*, **125**(1), pp. 183-192.
- [3] Shum, Y., Tan, C., and Cumpsty, N., 2000. "Impeller-diffuser interaction in a centrifugal compressor". *Journal of Turbomachinery*, **122**(4), pp. 777-786.
- [4] Sanders, A. J., and Fleeter, S., 1998. "Potential field interactions in a low-speed centrifugal compressor". *Journal of Propulsion and Power*, **14**(6), pp. 925-933.
- [5] Gaetani, P., Persico, G., Mora, A., Dossena, V., and Osnaghi, C., 2011. "Impeller-vaned diffuser interaction in a centrifugal compressor at the best efficiency point". In ASME Turbo Expo 2011: Turbine Technical Conference and Exposition, Vancouver, ASME Paper GT2011-46223.
- [6] Gaetani, P., Persico, G., Mora, A., Dossena, V., and Osnaghi, C., 2011. "Impeller-vaned diffuser interaction in a centrifugal compressor at off design conditions". In ASME Turbo Expo 2011: Turbine Technical Conference and Exposition, Vancouver, ASME Paper GT2011-46234.
- [7] Smythe, C. J., 2005. "Forced response predictions in modern centrifugal

- compressor design”. Master’s thesis, Massachusetts Institute of Technology.
- [8] Villanueva, V., 2006. “Characterization of the flow field response to vaneless space reduction in centrifugal compressors”. Master’s thesis, Massachusetts Institute of Technology.
- [9] Gould, K. A., Tan, C. S., and Macrorie, M., 2007. “Characterization of unsteady impeller-blade loading in a centrifugal compressor with a discrete-passage diffuser”. In ASME Turbo Expo 2007: Power for Land, Sea, and Air, Montreal, ASME Paper GT2007-28002.
- [10] Srivastava, R., Lentz, J., Liu, J. S., and Panovsky, J., 2007. “Computation of unsteady flow field and blade response due to impeller-diffuser interaction”. In ASME Turbo Expo 2007: Power for Land, Sea, and Air, Montreal, ASME Paper GT2007-28235.
- [11] Zemp, A., and Abhari, R. S., 2013. “Vaned diffuser induced impeller blade vibrations in a high-speed centrifugal compressor”. *Journal of Turbomachinery*, **135**(2), 021015.
- [12] Ziegler, K. U., 2003. “Experimentelle untersuchung der laufrad-diffusor-interaktion in einem radialverdichter variabler geometrie”. Doctoral Thesis *in german*, RWTH, Aachen, Germany.
- [13] Connell, S., Braaten, M., Zori, L., Steed, R., Hutchinson, B., and Cox, G., 2011. “A comparison of advanced numerical techniques to model transient flow in turbomachinery blade rows”. In ASME Turbo Expo 2011: Turbine Technical Conference and Exposition, Vancouver, ASME Paper GT2011-45820.

- [14] Connell, S., Hutchinson, B., Galpin, P., Campregher, R., and Godin, P., 2012. "The efficient computation of transient flow in turbine blade rows using transformation methods". In ASME Turbo Expo 2012: Turbine Technical Conference and Exposition, Copenhagen, ASME Paper GT2012-69019.
- [15] Liu, Y., Liu, B., and Lu, L., 2010. "Investigation of unsteady impeller-diffuser interaction in a transonic centrifugal compressor stage". In ASME Turbo Expo 2010: Power for Land, Sea, and Air, Glasgow, ASME Paper GT2010-22737.

초 록

비정상 전산유체해석을 이용하여 유량 계수가 임펠러 비정상 하중에 미치는 영향을 조사하였다. 이를 위해 세 개의 유량 계수(실속 근처, 설계점, 그리고 초크 근처)와 두 개의 래디얼갭(1.04와 1.10)에서 해석을 수행하였다. 계산 효율을 위해 푸리에 변환 방법을 사용하였으며 두 개의 임펠러와 디퓨저 유로에 대해서 비정상 해석을 수행하였다. 정상 해석과 비정상 해석 모두 실험 결과와의 비교를 통해 검증하였다. 래디얼갭이 1.04인 경우, 비정상 하중(하중의 최대값과 최소값의 차이)은 실속 근처, 초크 근처, 그리고 설계점 순서로 크며 유량 계수는 임펠러 압력면의 압력에 영향을 미친다. 설계점 대비 실속 근처의 경우 최소 하중이 더 작으며 초크 근처는 최대 하중이 더 크다. 그러므로 설계점 대비 실속 근처와 초크 근처에서 임펠러 비정상 하중이 더 크다. 이 차이는 디퓨저 베인 입구의 원주 방향 압력 불균일성에 기인하며 이는 디퓨저 베인 입사각에 의해서 결정된다. 래디얼갭이 1.10인 경우, 래디얼갭 1.04대비, 비정상 하중이 모든 유량 계수에서 감소하였으며 유량 계수가 비정상 하중에 미치는 영향이 미비하다. 이는 래디얼갭 증가에 따른 디퓨저 베인 잠재 효과의 감소에 기인한다.

주요어 : 원심압축기, 유량 계수, 비정상 전산유체역학, 비정상 하중

학 번 : 2016-20668